

FLAME SYNTHESIS OF TUNGSTEN-DOPED TITANIUM DIOXIDE NANOPARTICLES

By

YUQIAN ZHANG

A Thesis submitted to the

Graduate School-New Brunswick

Rutgers, The State University of New Jersey

in partial fulfillment of the requirements

for the degree of

Master of Science

Graduate Program in Mechanical and Aerospace Engineering

written under the direction of

Professor Stephen D. Tse

and approved by

New Brunswick, New Jersey

January 2016

ABSTRACT OF THE THESIS

FLAME SYNTHESIS OF TUNGSTEN-DOPED TITANIUM DIOXIDE NANOPARTICLES

By YUQIAN ZHANG

Thesis Director:

Professor Stephen D. Tse

Metal-doped titanium dioxide nanoparticles can be employed in various applications, including dye-sensitized solar cells and gas sensors. Metal-doping is able to enhance the performance of titanium dioxide as photocatalysts by the dispersion of metal ions into the TiO_2 matrix. In this work, tungsten-doped titanium dioxide nanoparticles are synthesized by a multiple diffusion flames burner using TTIP as the precursor (for titania) and tungsten mesh as the metal source (for doping). This novel method of using a metal mesh as precursor for doping is especially advantageous for low-vapor-pressure precursors and the entire nanoparticle synthesis process to be gas-phase based. The effect of varying the tungsten loading rate is studied for synthesizing doped titanium dioxide with different tungsten amount. The results show that high loading rate of tungsten can trigger homogenous nucleation of WO_3 prior to reaching the TTIP precursor loaded region, thereby leaving less tungsten ions to be doped into TiO_2 , when compared to the relatively lower tungsten loading rate configuration. Heat treatment at 973 K in an Ar atmosphere moves some of the tungsten out of the TiO_2 structure, thus making a new $\text{WO}_x\text{-TiO}_2$ solid solution, while tungsten ions are reduced to lower oxidation states. Moreover the annealing process also increases

the unit cell volume of W-doped TiO_2 , making the value closer to that of the un-doped TiO_2 . XRD, SEM, TEM, and XPS results are to prove the theory presented. UV Vis results show tungsten doping and heat treatment improve the absorbing ability of titanium dioxide in the visible light wavelength range significantly.

ACKNOWLEDGEMENTS

I would like to thank my advisor, Professor Stephen D. Tse, for all the support and guidance throughout the past two years. The experiment would never been successful without his help. During these two years, his enthusiastic guidance, insightful discussions, and expert advice always motivated me to be a researcher and engineer. I am also grateful to Professors Lin, Zadeh, and Kear for reviewing my thesis and providing me with their advice.

I really appreciate the help from all my lab mates throughout the work. I would like to thank Dr. Gang Xiong for helping me whenever I had problems with the experiment or the setup. His valuable insight helped me to gain a good understanding of the fundamentals of this research project. I would also like to thank Dr. Zhizhong Dong from the bottom of my heart for taking time out of his schedule every now and then to help me with the SEM, TEM, and XRD. He was always there discussing the results, sharing his valuable advice, and consistently encouraging me. Without their selfless help, I don't know if I would even graduate. I would like to thank Hua Hong for his help when I came to the lab and built the setup. I also thank all the other members of our group for making the two years so amazing for me.

Especially, I want to thank my parents. Without their endless support and encouragement, I would not have been able to come to the United States, not to mention earning the degree.

Table of Contents

ABSTRACT OF THE THESIS	ii
ACKNOWLEDGEMENTS	iii
LISTS OF TABLES	vii
LIST OF FIGURES	vii
Chapter 1 Introduction and Literature Review	1
1.1 Introduction	1
1.2 TiO ₂ Background	1
1.2.1 TiO ₂ structure and properties.....	1
1.2.2 TiO ₂ Synthesis.....	6
1.3 Doped TiO ₂ background.....	7
1.3.1 Doped TiO ₂ Mechanism.....	7
1.3.2 Doped TiO ₂ Synthesis	8
1.4 Application of TiO ₂ and doped TiO ₂ nanoparticles.....	9
1.4.1 Wastewater treatment.....	9
1.4.2 Dye-Sensitized TiO ₂ in water splitting and solar cells.....	10
1.4.3 Sensors	11
1.5 Flame synthesis for undoped and doped TiO ₂ nanoparticles	11
1.6 Summary and overview of the thesis	13
Chapter 2 Experimental Setup	15
2.1 Multiple-diffusion flames burner setup	15

2.2 Substrate Setup	17
2.3 Mass flow Controllers Setup	18
2.4 Precursor System Setup	19
2.5. Experimental Procedure	20
Chapter 3 Ex-situ Characterizations	22
3.1 X-Ray Diffraction (XRD).....	22
3.2 Transmission Electron Microscopy (TEM).....	23
3.3 Field Emission Scanning Electron Microscope (FESEM) and Energy-dispersive X-ray spectroscopy (EDS)	23
Chapter 4 Results and Discussion.....	24
4.1 Introduction	24
4.2 XRD Results and Discussion.....	24
4.2.1 XRD results	24
4.2.2 XRD results discussion	30
4.3 SEM and EDS Results and Discussion.....	35
4.4 XPS Results and Discussion.....	39
4.5 TEM Results and Discussion.....	41
4.6 Uv-Vis Results and Discussion	43
Chapter 5 Conclusions and Future Scope	46
5.1 Conclusions	46
5.2 Future Scope	46
Chapter 6 References	48

LISTS OF TABLES

Table 1.1 Crystal structure data for $\text{TiO}_2^{5,6,7}$	2
Table 1.2 Synthesis method of doped TiO_2	8
Table 1.3 A list of TiO_2 flame synthesis set-up	12
Table 2.1 Parameters of the gases	18
Table 4.1 Weight and atomic percentage of tungsten	39
Table 4.2 Measured d -spacing of 1W- TiO_2	43
Table 4.3 d -spacing of un-doped TiO_2	43

LIST OF FIGURES

Fig 1.1 Crystal structures of the rutile and anatase phase of TiO_2^8	3
Fig 1.2 lattice structure of brookite TiO_2	3
Fig 1.3 Mechanism of light absorption by TiO_2^{15}	5
Fig 1.4 Surface band bending of the anatase and rutile phases of TiO_2^{16}	5
Fig 2.1 Schematic of the burner	16
Fig 2.2 Top-view of the burner	17
Fig 2.3 precursor bubbler design	20
Fig 4.1 XRD pattern of as-synthesized and calcined doped/un-doped TiO_2	25
Fig 4.2 enlarged anatase (101) and rutile (110) peak	26
Fig 4.3a anatase parameter a	27
Fig 4.3b anatase parameter c	27
Fig 4.3c rutile parameter a	28

Fig 4.3d rutile parameter c	28
Fig 4.3e Anatase unit cell volume	29
Fig 4.3f Rutile unit cell volume	29
Fig 4.5 Particle formation and growth mechanisms ⁷²	31
Fig 4.5a Heterogeneous nucleation using single layer W mesh	33
Fig 4.5b Homogenous nucleation using double layers W mesh	34
Fig 4.6a SEM image of un-doped TiO ₂	35
Fig 4.6b SEM images of TiO ₂ -1W (left) and HT-TiO ₂ -1W (right)	36
Fig 4.6c SEM images of TiO ₂ -2W (left) and HT-TiO ₂ -2W (right)	36
Fig 4.7 EDS spectrum of (a) un-doped TiO ₂ , (b) TiO ₂ -1W, (c) HT-TiO ₂ -1W, (d) TiO ₂ -2W, (e) HT-TiO ₂ -2W	38
Fig 4.8a XPS spectra of W 4f core level of 1W-TiO ₂	40
Fig 4.8b XPs spectra of W 4f core level of HT-1W-TiO ₂	41
Fig4.9a TEM images of 1W-TiO ₂ nanoparticles	42
Fig 4.9b SAED patterns of 1W-TiO ₂ nanoparticles	42
Fig 4.10a Tauc plot of un-doped TiO ₂	43
Fig 4.10b Tauc plot of 1W-TiO ₂	44
Fig 4.10c Tauc plot of HT-1W-TiO ₂	44

Chapter 1

Introduction and Literature Review

1.1 Introduction

Since the Honda-Fujishima effect was discovered by Fujishima et al¹ in 1972, titanium dioxide has become one of the most widely investigated photocatalysts. Compared to bulk materials, TiO₂ nanoparticles have unique properties for low cost, chemical reactivity, and enhanced plasticity. These properties make TiO₂ nanomaterials useful in many applications, such as chemical gas sensors, thermal barrier coatings, photovoltaics, catalysts and catalyst-supports. All these properties can mainly be attributed to the high specific surface area of nanoparticles when compared to their corresponding bulk material forms.

W-doped TiO₂ nanoparticles are the main study of this work. Enhanced properties are found compared to pure TiO₂ nanoparticles. The background and applications of pure and doped TiO₂ nanomaterials are addressed in this chapter. The experiment set up and procedures are addressed in later sections followed by results and discussion; and conclusion and future scope.

1.2 TiO₂ Background

1.2.1 TiO₂ structure and properties

In nature, titanium dioxide is usually found in three crystalline phases: anatase (tetragonal), brookite (orthorhombic), rutile (tetragonal)². Rutile is the stable phase and the most commonly found form of titanium oxide in nature, but anatase and brookite are more common in synthetic and nanoscale samples. These crystalline phases of TiO₂ transform to rutile at temperature > 973 K at atmospheric pressure^{3,4}.

Table 1.1 Crystal structure data for TiO₂^{5,6,7}

Properties	Rutile	Anatase	Brookite
Crystal structure	Tetragonal	Tetragonal	Orthorhombic
Lattice constant (Å)	$a = 4.5936$ $c = 2.9587$	$a = 3.784$ $c = 9.515$	$a = 9.184$ $b = 5.447$ $c = 5.154$
Space group	P4 ₂ /mm	I4 ₁ /amd	Pbca
Molecule (cell)	2	2	4
Volume/ molecule (Å ³)	31.2160	34.061	32.172
Density (g cm ⁻³)	4.13	3.79	3.99
Ti–O bond length (Å)	1.949 (4) 1.980 (2)	1.937(4) 1.965(2)	1.87–2.04
O–Ti–O bond angle	81.2° 90.0°	77.7° 92.6°	77.0°–105°

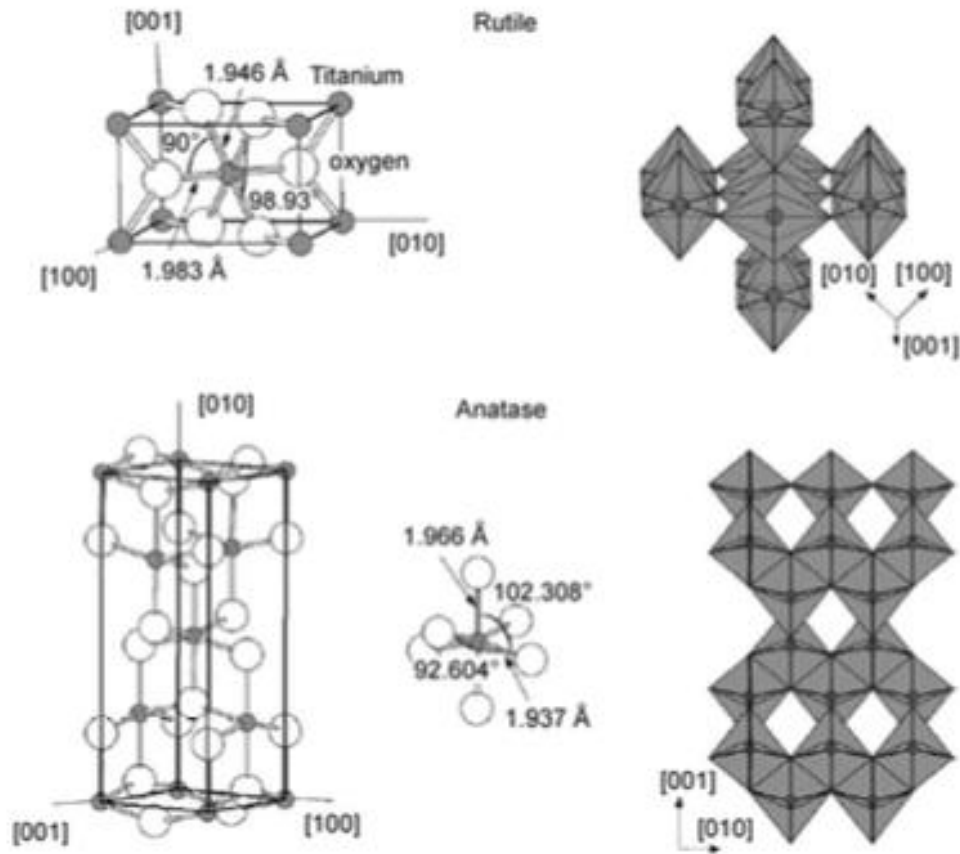


FIGURE 1.1 Crystal structures of the rutile and anatase phase of TiO_2 ⁸

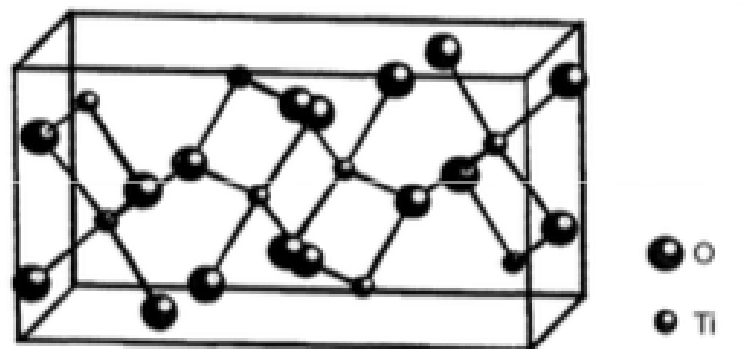


FIGURE 1.2 lattice structure of brookite TiO_2

Rutile: Rutile TiO_2 has a tetragonal structure and contains 6 atoms per unit cell (**Figure 1.1**). The TiO_6 octahedron is slightly distorted^{8,9,10}. The rutile phase is found to be stable at most temperatures and pressures up to 60 kbar. Anatase and brookite phases convert to the rutile phase after reaching a certain particle size, with the rutile phase being more stable than anatase for particle sizes greater than 14nm¹¹. After the rutile phase is formed, it grows much faster than the anatase phase. The activity of the rutile phase as a photocatalyst is usually very poor. However, Sclafani et al¹² found that the rutile phase can be active or inactive, depending on its preparation conditions.

Anatase: Anatase TiO_2 also has a tetragonal structure, but the octahedron is significantly distorted so that its symmetry is lower than orthorhombic, as shown in **Figure 1.1**. The anatase phase is found to be more stable than the rutile phase at 0 K with a small energy difference, according to Muscat's research¹³. Considering its higher electron mobility, low dielectric constant, and lower density, the anatase structure is favored over other polymorphs for solar cell applications. The anatase phase has a higher photoreactivity due to the higher Fermi level, lower capacity to absorb oxygen, and higher degree of hydroxylation¹⁴.

Brookite: Brookite TiO_2 has an orthorhombic crystal system. The unit cell is formed by edge-sharing TiO_6 octahedra and composed of eight formula units of TiO_2 (**Figure 1.2**). It has a larger cell volume and is more complicated. It received less experimental study compared with the other two phases.

Anatase TiO_2 is considered as an active photocatalyst under UV light. When exposed to UV light, electrons in the valence band are excited to the conduction band leaving behind holes,

as shown in **Figure 1.3**. Its inherent surface band bending forms spontaneously in a deeper region with a steeper potential compared with the rutile phase, as shown in **Figure 1.4**.

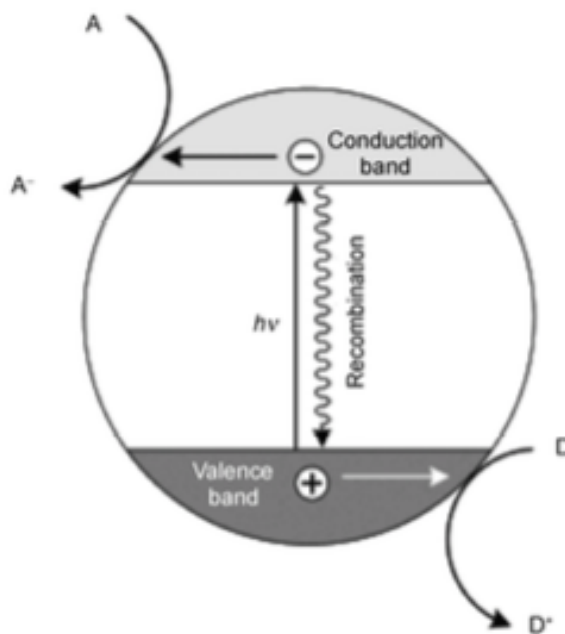


Figure 1.3 Mechanism of light absorption by TiO_2 ¹⁵

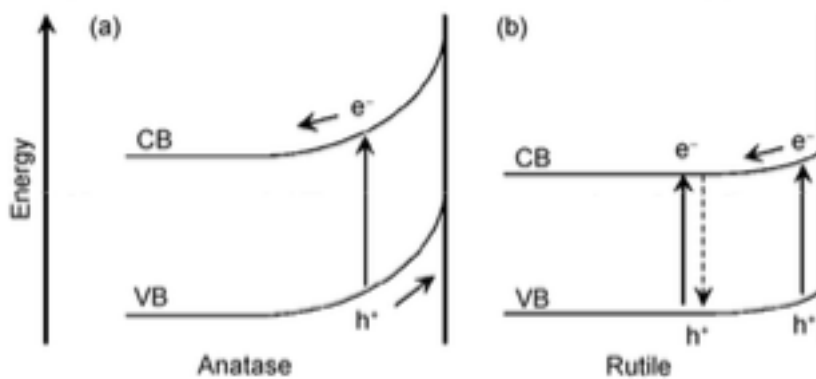


Figure 1.4 Surface band bending of the anatase and rutile phases of TiO_2 ¹⁶

1.2.2 TiO₂ Synthesis

Various methods have been used and developed to produce TiO₂ nanoparticles. Clearly from different methods, nanoparticles of TiO₂ are obtained in different phases, morphology, structures, and particle sizes.

The sol-gel method is a common process for making many ceramic materials^{17,18}. TiO₂ nanoparticles have been produced with the sol-gel method from hydrolysis of a titanium precursor¹⁹. This process normally proceeds via an acid-catalyzed hydrolysis step of titanium alkoxide followed by condensation. Also highly crystalline anatase TiO₂ nanoparticles in different sizes and shapes can be obtained by the polycondensation of titanium alkoxide in the presence of tetramethylammonium hydroxide^{20,21}. Sugimoto concluded that by tuning the reaction parameters in the sol-gel method, TiO₂ nanoparticles of different sizes and shapes can be formed^{22,23}. By adding HClO₄ or NaOH solution, the pH of the solution can be tuned. At pH above 11, the morphology of the TiO₂ nanoparticles converts from cuboidal to ellipsoidal. By heating the as-prepared gel over a certain time below 100°C, the agglomeration of the TiO₂ nanoparticles during the crystallization process can be avoided^{24,25}. According to Zhang and Banfield, large quantities of single-phase anatase TiO₂ nanoparticles with average sizes between 7 to 50 nm can be obtained by heating amorphous TiO₂ in air^{26,27,28,29}. Other sol-gel modifications, such as a semi-continuous reaction method by Znaidi et al³⁰, a continuous reaction method, and a two-stage mixed method by Kim et al³¹, have been used to achieve highly crystallized and narrowly-dispersed TiO₂ nanoparticles.

Another important method of synthesis of titania nanoparticles is flame synthesis. By controlling the precursor loading rate, the substrate temperature, the temperature time history of the particles, and other factors, TiO₂ nanoparticles with different properties and characteristics like size, morphology and structure can be produced. The details of the flame synthesis method is presented in a later section.

Apart from the methods mentioned above, other methods, such as micelle and inverse micelle, hydrothermal, solvothermal, direct oxidation, chemical vapor deposition, and physical vapor deposition, are also used for the synthesis of titanium dioxide nanostructured materials⁹.

1.3 Doped TiO₂ background

1.3.1 Doped TiO₂ Mechanism

Over the past decades, doped TiO₂ nanomaterials have been widely studied for enhanced photocatalytic performance under visible light irradiation and on the degradation of various organic pollutants. Different transition metals such as Cu, Co, Ni, Cr, Mn, Mo, Nb, V, Fe, Ru, Au, Ag, Pt, W^{15,32,33,34,35} and non-metal elements such as N, S, C, B, P, I, F^{36,37,38} have been doped into TiO₂ nanoparticles by different approaches.

Choi et al³³ had a systematic study on the photocatalytic activity of TiO₂ nanoparticles doped 21 different ions. When doped with Fe³⁺, Mo⁵⁺, Ru³⁺, Os³⁺ and V⁴⁺, a significantly increase in the photoreactivity for the reduction of CCl₄ and the oxidation of CHCl₃ was observed. Due to the formation of a new energy level production of TiO₂ by doping the metal nanoparticles into the TiO₂ matrix, the visible light photoactivity of metal-doped TiO₂ is increased. The transition metals play an important role as electron traps that prevent or mitigate electron-hole recombination to

increase the number of electrons flowing to another electrode in order to improve the photoreactivity of TiO_2 ³⁹. Zhao et al⁴⁰ investigated N- TiO_2 and raised opinions on a modification mechanism of non-metal doped TiO_2 , which involves: (1) band-gap narrowing caused by high nitrogen doping; (2) oxygen vacancies formed easier in N- TiO_2 than pure TiO_2 which enhance the visible activity; (3) impurity-energy levels induced above the band gap by low nitrogen doping.

1.3.2 Doped TiO_2 Synthesis

To improve the photocatalytic effect in the visible light region, a lot of methods were successful in doping trace impurity into TiO_2 including plasma, ion-assisted sputtering, chemical vapor deposition (CVD) and sol-gel. A list of metallic and non-metallic doped TiO_2 and methods of the preparation are shown in **Table 1.2**.

Table 1.2 Synthesis method of doped TiO_2

Kind of dopant	Doped element	Preparation method	Reference
metal	Ag	Reduction agent was mixed with silver nitrate. The reaction temperature was raised to 80°C with stirring. TTIP and HNO_3 were added and kept the reaction temperature at 50°C for 24 h and calcined at 300°C.	41
	Fe	Flame spray synthesis: 99.9% iron pieces and 99.99% titanium target were placed in a reaction chamber and a mixture of oxygen and argon was ejected into the chamber during the discharging	42
	W	Sol-gel method: Solution 1 (TiCl_4 in distilled water) was mixed with solution 2 (H_2WO_4 and $(\text{NH}_4)_6\text{H}_2\text{W}_{12}\text{O}_{40}$ in water along with ethanol. Stirring 15 h at room temperature and heated the solution at 353K for 1.5 h and calcined at 353K.)	43

	Pt	Photo reduction process: TiO_2 suspended in a mixture of hexachloroplatinic acid in methanol. Irradiated the suspension with a 125 W mercury lamp for an hour. Separated the Pt- TiO_2 by filtration, washed with distilled water and dried at 100°C for 24 h.	44
	Au	Titanium butoxide dissolved in ethanol was added to solution containing tetrachloroauric acid, acetic acid and ethanol. The result suspension was aged for 2 days, dried under vacuum, grinded and calcined at 650°C .	45
nonmetal	N	TiN oxidation: Heat the TiN at 450°C - 550°C for 2 h in air with heating rate $2^\circ\text{C}/\text{min}$.	46
		Treating anatase TiO_2 powder in Ar atmosphere at 600°C for 3 h.	47
	S	Oxidation annealing TiS_2 at 300 - 600°C	48
	C	Alkoxide precursor dissolved in corresponding alcohol, mixed with Hydrochloric acid aqueous solution. Gel was aged for several days, calcined in air and grounded.	49
	B	Grinding the anatase TiO_2 powder with boric acid and calcined in air at 450°C .	50
	P	Hydrolyzed TTIP in the mixture of isopropanol and water. Stirred for 2h, centrifuged at 3500 rpm and dried at 100°C . Calcined the powder at 300°C .	51

1.4 Application of TiO_2 and doped TiO_2 nanoparticles

1.4.1 Wastewater treatment

Over the past two decades, TiO₂ nanoparticles have been proved useful for the degradation of wastewater pollutants. Water contaminated with organic species and metal were treated with TiO₂ by Piairie et al⁵² and they found that Ag⁺, Hg²⁺, Cr⁶⁺ and Pt²⁺ were easily treated by photocatalytic reduction with 0.1 wt% TiO₂ while Cd²⁺, Cu²⁺ and Ni²⁺ stayed. The ability of TiO₂ in removing the metal ions depend on the standard reduction potential of the metal. Mahmoodi et al⁵³ concluded that immobilized TiO₂ nanoparticles were able to degrade the Acid Blue 25 in textile wastewater thus reducing its toxicity. Also Asmussen et al⁵⁴ used bifunctional electrodes that performed both electrochemical oxidation and photocatalytic degradation in waste water remediation where a thin film of TiO₂ was coated on one side of a Ti plate.

1.4.2 Dye-Sensitized TiO₂ in water splitting and solar cells

Dye-sensitized TiO₂ has drawn much attention in photovoltaic applications in recent years. TiO₂ catalysts are able to make full use of visible light to realize photocatalytic reactions when sensitized by dyes. Chemisorbed or physisorbed dye-sensitized TiO₂ has an increased efficiency of the excitation process and an expanded wavelength range of excitation for the photocatalyst comparing to the pure TiO₂, which is a wide band gap semiconductor. Duonghong et al⁵⁵ found the TiO₂ loaded with ultrafine Pt and RuO₂ showed highly activity as an H₂O decomposition catalyst under the band gap excitation of the TiO₂. Abe et al⁵⁶ found Ru complex dye N3 dye-sensitized Pt/TiO₂ an effective photocatalysts in water splitting. The rates of H₂ evolution decreased with an increased proportion of water in the water-acetonitrile solution because the decrease in the energy gap between the redox potential led to a decreased efficiency of electron transfer to the dye. Considering the significantly enhanced light absorption efficiency, Gratzel⁵⁷

developed a highly porous TiO₂ substrate containing a coumarin dye serving as the sensitizer which are a far cheaper alternative to amorphous silicon solar cells.

1.4.3 Sensors

TiO₂ nanomaterials have been widely used as sensors for various gases. Grimes et al⁵⁸ had a series of studies on using TiO₂ nanotubes as excellent room-temperature hydrogen sensors with a high sensitivity of 10^4 along with the ability to self-clean photoactively after environmental contamination. Even after being extinguished by a rather extreme means of contamination such as immersed in motor oil, the H₂ sensing capabilities of the sensors were able to be mostly recovered by UV light exposure. TiO₂ nanomaterials are also used as oxygen sensors by Sotter et al⁵⁹. Oxygen vacancies formed by photo radiation acted as oxygen-sensing sites are found in Ta-doped TiO₂ sensors. Furthermore Ruiz et al⁶⁰ found La-doped TiO₂ nanomaterials made perfect sensing materials for ethanol based on electrical resistance while Co-doped TiO₂ nanoparticles were promising candidates for CO sensing. W-doped TiO₂⁶¹ was also found to have better performance in ethanol sensing than pure TiO₂.

1.5 Flame synthesis for undoped and doped TiO₂ nanoparticles

Flame synthesis, a \$15 billion/year industry, is currently a cost-effective manufacturing process for nanoparticles. It has been proven that the size, structure, and other characteristics of the as-synthesized nanoparticles can be controlled by modifying the reactor's operational parameters, including the fuel-to-oxidizer ratio and the precursor loading rate in the flame synthesis method.

A number of flame synthesis configurations have been used for the synthesis of TiO₂ nanoparticles, including co-flow diffusion flame, premixed flame, counter flow diffusion, and

premixed stagnation. Also a variety of fuels have been used in a wide range of temperatures along with different precursors like TiCl_4 and TTIP. A substrate placed downstream from the flame is commonly used to collect the particles. A summary of TiO_2 flame synthesis studies is given in

Table 1.3.

Table 1.3 A list of TiO_2 flame synthesis set-up

Author	Burner Type	Fuel/oxidizer/f lame temp($^{\circ}\text{C}$)	Precursor and carrier gas	Crystalline phase, morphology, size
Zhao et al ⁶²	Low pressure premixed stagnation flame	$\text{H}_2/\text{O}_2/<1150$	TTIP with N_2	Anatase particles with a primary size between 4 and 8nm.
Wang et al ⁶³	Premixed stagnation swirl flame	$\text{CH}_4/\text{O}_2/<1600$	TTIP with N_2	Pure anatase with diameter between 5-10 nm
Pratsin is et al ⁶⁴	Co-flow diffusion	$\text{CH}_4/\text{Air}/\sim 900$ - 1000	TiCl_4 with Ar	Mainly anatase with rutile ratio varying from 0.1 to 15 wt.% and particle size between 10 to 120 nm
Yeh et al ⁶⁵	Premixed flame	$\text{CH}_4/\text{O}_2 +$ $\text{N}_2/<1150$	TTIP with Air	Anatase ratio varies from 15 to 90 wt.% with particle size from 20 to 250 nm
Hung and Katz ⁶⁶	Counterflow diffusion	$\text{H}_2 + \text{Ar}/ \text{O}_2 +$ $\text{Ar}/ <\sim 1750$	TiCl_4 with $\text{H}_2 +$ Ar or $\text{O}_2 + \text{Ar}$	Anatase when using O_2 and rutile when using the H_2 . Particle size within 10-60 nm
George et al ⁶⁷	Premixed multiorfice burner	$\text{CO}/\text{O}_2/<1400$	TiCl_4 with premixed fuel	Size within 41-63 nm

McCor mick et al ⁶⁸	Premixed stagnation flame	$C_2H_4/O_2 +$ Ar/<1650	TTIP with Ar	Ultrafine anatase with size 3 to 6 nm
Bhanw ala et ⁶⁹ al	Co-flow diffusion	Liquid petroleum gas/ O_2	$TiCl_4$ with N_2	Pure anatase particles with average diameter of 104 nm
Fotou et al ⁷⁰	Co-flow diffusion	$CH_4/Air/\sim 900-$ 1150	$TiCl_4$ with Ar	Primarily anatase
Akurati et al ⁷¹	Co-flow diffusion	CH_4/O_2	TTIP with N_2	Mainly anatase phase (60-100 wt%). Particle size between 27 to 72 nm

As seen from the **Table 1.3**, TiO_2 nanoparticles can be produced in different phases and sizes by different kind of flames. However, as discussed in the previous sections, most doped- TiO_2 nanoparticles are synthesized from sol-gel, hydrothermal, or wet-chemistry methods, where the as-synthesized particles need post treatment and some time to form.

The unique synthesis configuration used in this work is a multi-element diffusion flame burner, where a larger diameter center tube, for the TTIP precursor, extends out of the honeycomb which is used for aligning the needle tubes. By using diffusion flames, limitations related to premixed flames such as flashback and flame speed can be avoided. The mixing of the fuel, oxidizer, and precursor are external to the burner so that unwanted reactions are avoided. Moreover, since the dopant metal mesh is placed on the tips of the arrays of diffusion flames, it gives the metal particles enough time and space to react with the TTIP flame. Finally, the burner is also capable of a larger-scale production of ready-to-use TiO_2 nanomaterials.

1.6 Summary and overview of the thesis

As seen from the research, over the past few decades, non-stop breakthroughs in the synthesis and modification of TiO_2 have resulted in new properties and applications with enhanced performance. Both doped and un-doped TiO_2 nanoparticles can be synthesized by different approaches with different particle sizes and phases with different properties. Comparing to other synthesis methods, the flame synthesis method draws the attention of researchers because of its advantages, including scalability, cost effectiveness, and purity.

In this thesis, a multiple diffusion flame burner is used to synthesize tungsten-doped titanium dioxide using TTIP as the precursor and tungsten mesh as the doping metal source. The effect of different loading rates of tungsten is studied by using single or double layers of tungsten mesh. Also the influence of heat treatment in an Ar atmosphere at 973K is also investigated. Ex-situ characterization is performed on the powders to discern the structures, phases, elemental compositions, and other properties of the nanoparticles. The thesis explains in detail the experimental setup; procedures of the experiment; results and discussion; and conclusions and future scope.

Chapter 2

Experimental Setup

2.1 Multiple-diffusion flames burner setup

Characterizing the multiple-diffusion flames burner, also known as a multi-element diffusion flame burner (MEDB, Hencken Burner) (**Fig 2.1**), each individual diffusion flame is run in the normal configuration, and a larger center tube carrying only fuel is seeded with precursor. Fuel (e.g. H_2 or CH_4) enters through the small stainless steel tubes, while the oxidizer (e.g. O_2 or air) along with the carrier gas (e.g. Ar) flows around the tubes. The top-view of the burner is shown in **Fig 2.2**, where a honeycomb is used to align the needle tubes. The fuel flows in the channels with an inserted tube, while the oxidizer flows in all empty channels; and the precursor gas (TTIP) flows through the center tube along with fuel. The OD and ID are 0.0280 and 0.0200 inch for the small tubing, respectively, while 0.25 and 0.22 inch for the center tube. The center tube extends 1 cm out of the honeycomb. The burner is made out of a 6 inch long ϕ 4 inch aluminum rod. The honeycomb is 2.5×2.5 inches while the tubing area is 1.5×1.5 inches. During the experiment, the metal source is placed 1mm above the honeycomb.

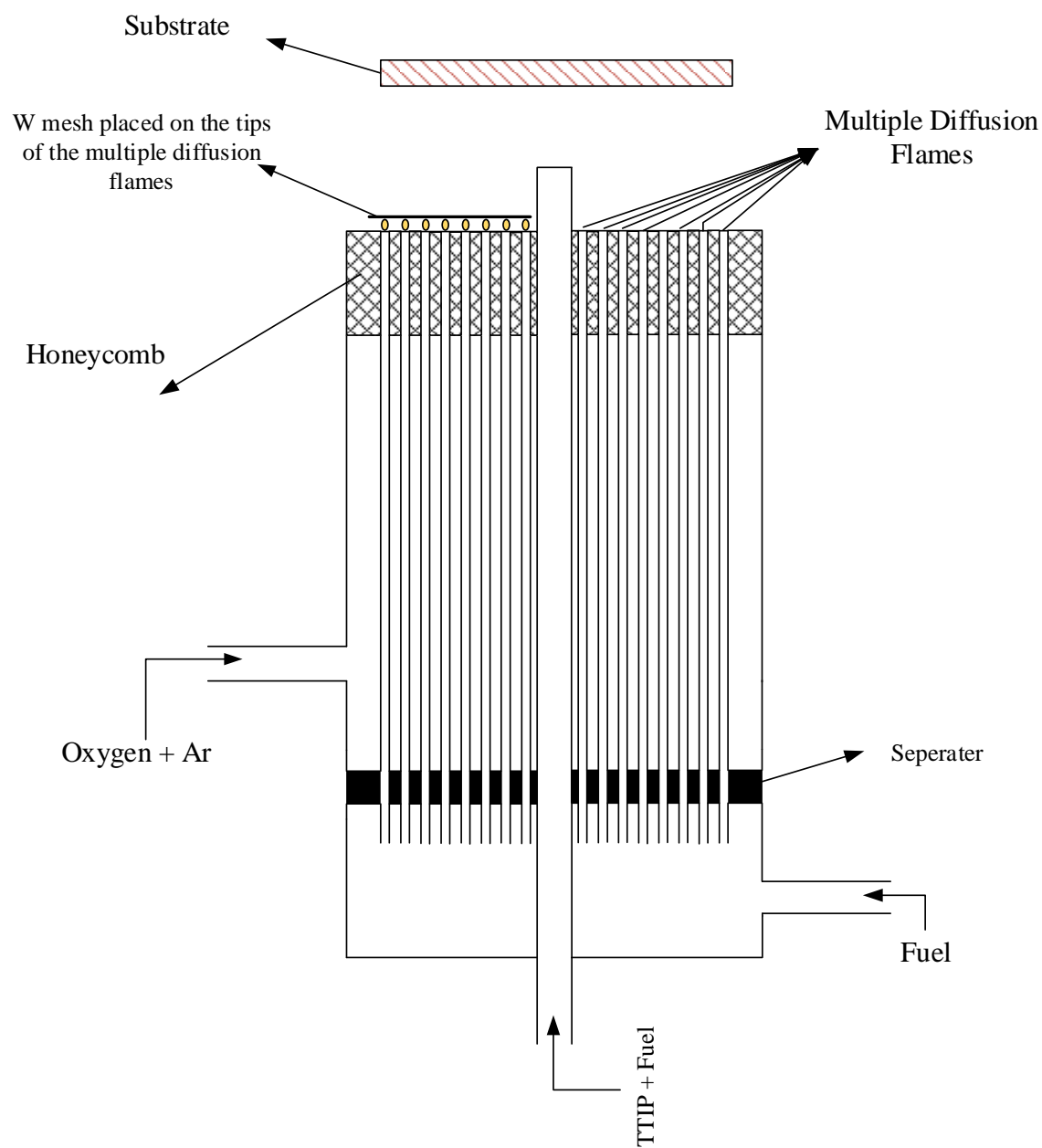


Fig 2.1 Schematic of the burner

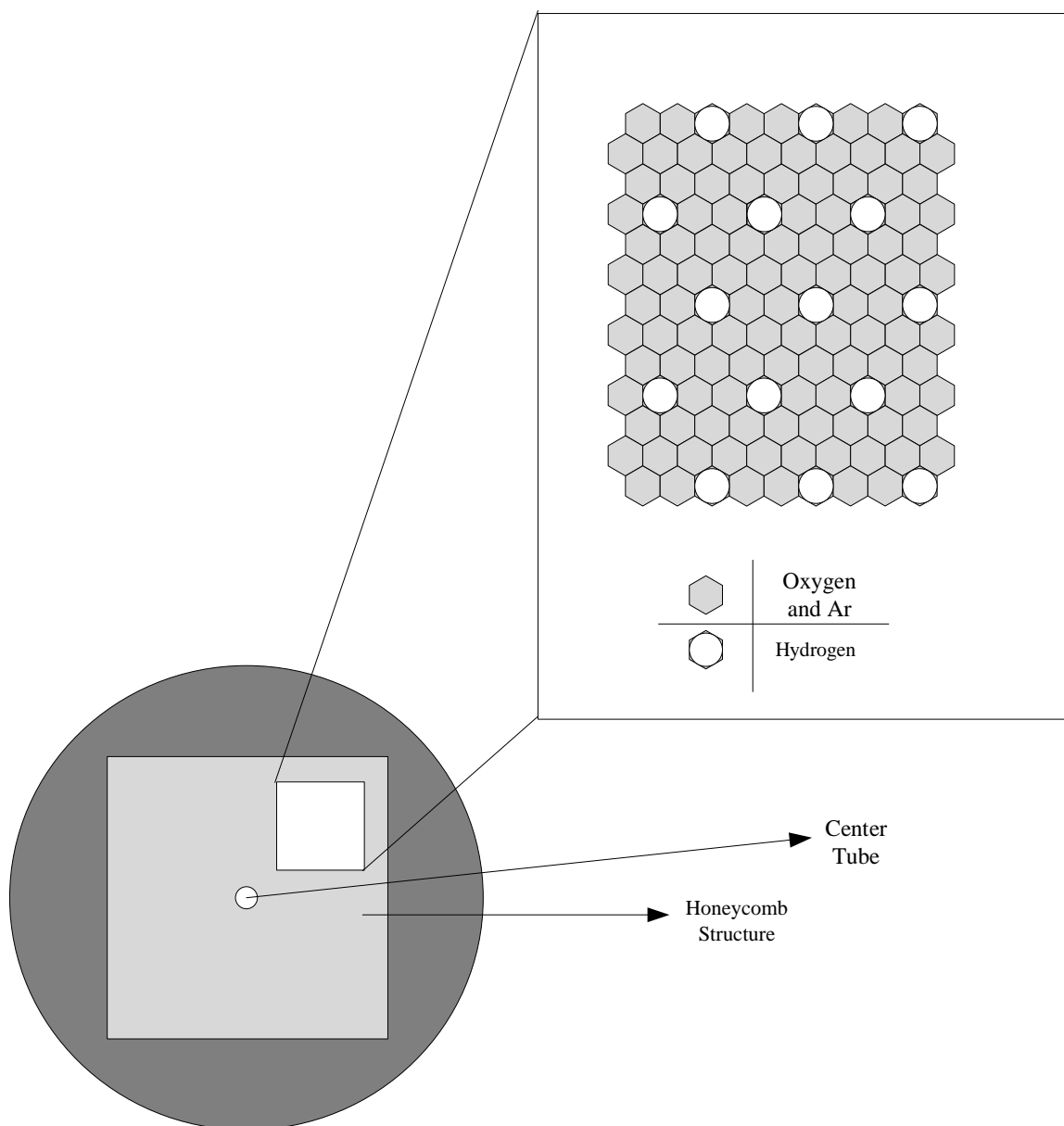


Fig 2.2 Top-view of the burner

2.2 Substrate Setup

A brushed finish 6 inch \times 6 inch \times 0.1 inch aluminum plate (from McMaster-Carr) is used as the substrate where the nanoparticles are grown. A cooling plate (from McMaster-Carr) is placed below the substrate with thermal grease (from Omega) applied between the layers to increase the

thermal conductivity. The cooling plate is made out of a 6 inch \times 6 inch \times 0.75 inch aluminum plate. It has cooling water circulating through with a flow rate controlled by a valve to adjust its temperature of the substrate. A K-type thermocouple (from Omega) is inserted in-between the cooling plate and the substrate to monitor the temperature. The whole substrate setup is mounted on a truss platform so the distance between the substrate and the flame can be adjusted.

2.3 Mass flow Controllers Setup

Mass flow controllers (MFCs) are used to precisely regulate the gas flow rates. Digital command modules from AALBORG are used to control the MFCs, which ensures the reproducibility of the experiment and reduces any experimental error. It generates a 0-5V signal which is directly proportional to the flow rate of gases through the controllers. A percent value set for the gases can be entered in the command module which allows the same percent of gas of the total flow rate of the MFC to pass through it. The setup is placed onto an optical table, where it can be easily moved in any direction. The percent set for the gases and their resultant flow rates are shown in the following table. The details of the precursor lines will be presented in later section. **Table 2.1** shows the parameters used for this experiment.

Gas	Controller range	Percent set	Flow rate
H ₂	5 slpm	40%	2L/min
O ₂	10 slpm	80%	8L/min
Ar	20 slpm	50%	10L/min
Ar (precursor line)	2 slpm	21.5%	0.425L/min
H ₂ (precursor line)	500 sccm	20%	0.1L/min

Table 2.1 Parameters of the gases

2.4 Precursor System Setup

The core part of the precursor system is the bubbler. Titanium tetraisopropoxide (TTIP) from Sigma Aldrich with 97% purity is the precursor used for the experiment. The precursor kept in the bubbler is radiantly heated up to 100°C. The heater for the bubbler only takes current input within 4 to 20 mA, so a SCR from Omega Engineering and a transmitter from Weidmuller are connected between the heater and the temperature controller. The SCR converts the signal from the temperature controller into a voltage signal within the range 0 to 10 V, and furthermore the transmitter converts the voltage signal into the current signal to control the temperature of the heater. The carrier gas used for the TTIP line is argon and hydrogen which directly goes to the center tube. To prevent condensation of the precursor in the line, all lines are heated up to 130°C with rope heaters from McMaster-Carr. Also, all precursor lines are wrapped by thermal insulation material from McMaster-Carr to reduce heat loss to the ambient atmosphere. Several K-type thermocouples are used to measure the temperature of the precursor line, and temperature controllers from Omega Engineering are used to maintain the temperature. Valves are used upstream where the carrier gas combines with the TTIP to protect against gas flow back into the MFCs. As shown in **Fig 2.3**. When flame is ignited, bypass line 1 is kept open. After the flame becomes stable, valve 2 downstream from the bubbler is opened. Finally, valve 3 is slowly opened while valve 1 is slowly closed. The last two procedures need to be done slowly to avoid a large amount of TTIP from going through the center tube, in which case the flame would not stay stable. For the shutdown process, the procedures are reversed. First switch on valve 1 and then close valve 2 and 3. The order is important prevent TTIP contamination of the MFCs.

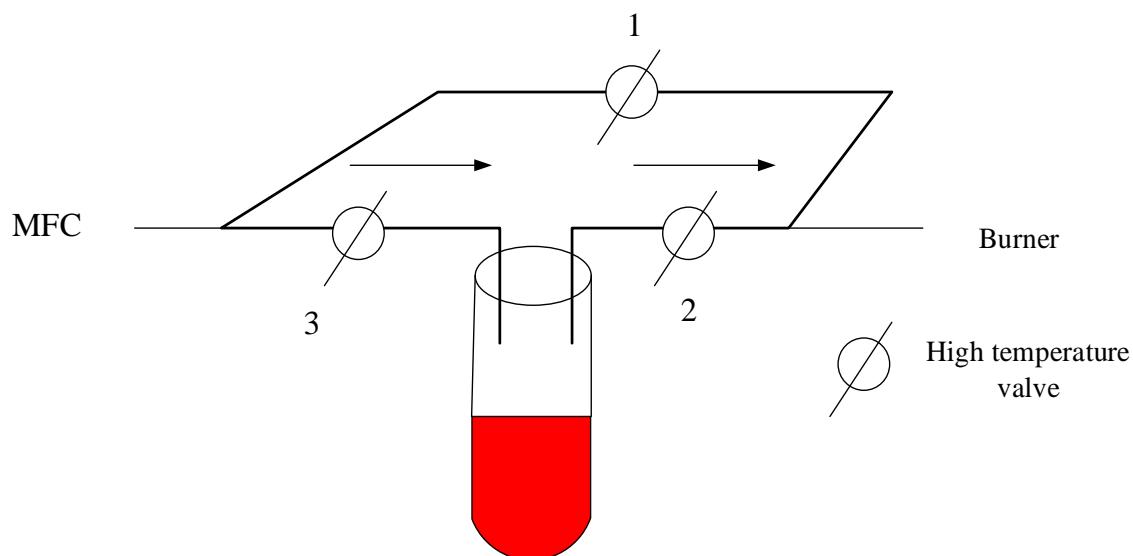


Fig 2.3 precursor bubbler design

2.5. Experimental Procedure

1. Start the cooling water for the substrate.
2. Place the metal mesh in position.
3. Turn on the rope heaters for the lines.
4. Turn on the heater for the bubbler.
5. Open the gas tank and set the controllers of all gas lines to the value mentioned earlier.
6. Make sure all the connections are grounded.

7. Preheat for about 10-15 minutes. When all lines are warmed up to the desired temperature, open valve 1 of the bubbler and the valves in other gas lines to start the gas flow.
8. Make sure all the flow rates are constant.
9. Put the substrate on.
10. Ignite the flame.
11. Place the hood on.
12. Water will be condensed on the substrate before it is heated up. Wait until all the water is vaporized.
13. When the water on the substrate is all vaporized, slowly open the valve 2 and 3 then slowly close the valve 1.
14. Start the timer and run the experiment for the desired time depending on the case.
15. When the timer stops, take the substrate off first.
16. Open bubbler valve 1 and then close valve 2 and 3.
17. Turn off all the heaters.
18. Turn off the valves of the gas lines
19. Turn off the MFCs.
20. Close all the gas tanks.
21. Let the setup cool down.
22. Collect the TiO_2 powders on the substrate carefully and store them in a case, along with proper tag.

Chapter 3

Ex-situ Characterizations

3.1 X-Ray Diffraction (XRD)

XRD is essential in the determination of the crystal structure and the composition of the metal-doped TiO₂ nanoparticles. The unit cell volume can be estimated based on the Bragg equation:

$$n\lambda = 2d \sin \theta,$$

where θ is the half value of the diffraction angle, λ is the wavelength of the X-ray radiation and d is d -spacing. As CuK α 1 is being used as the diffraction wave, λ here is 1.5436 Å. Furthermore, since both anatase and rutile phase TiO₂ are tetragonal, we have

$$\frac{1}{d^2} = \frac{h^2 + k^2}{a^2} + \frac{l^2}{c^2}$$

$$V_{\text{cell}} = a^2c$$

Where h , k , l are the Miller indices which correspond to the diffraction angle; a and c are the parameters of the TiO₂ nanostructure. V_{cell} is the unit cell volume.

The grain size is determined by measuring the broadening of a particular peak in a diffraction pattern connected with a specific planar reflection from within the unit crystal cell. In this study, A Siemens D500 X-ray Diffractometer is used. The nanoparticles taken from the substrate are put inside a circular indentation of a disc and a drop of ethyl alcohol is added to make

the powders form a thin layer. Each case is run for 15 minutes. The analysis gives the composition of the particles as well as the average diameter of the sample particles.

3.2 Transmission Electron Microscopy (TEM)

TEM (TOPCON 002B) is where a beam of electrons is transmitted through an ultra-thin layer of sample. The morphologies and the grain sizes of the nanoparticles are determined. High resolution transmission electron microscopy (HRTEM) is also used to examine the atomic-level structures of the particles. Selected area diffraction (SAD) can be performed to evaluate the phase composition of single or a small group of nanoparticles.

3.3 Field Emission Scanning Electron Microscope (FESEM) and Energy-dispersive X-ray spectroscopy (EDS)

FESEM is used for imaging a sample by scanning it with a beam of electrons. The interaction between the electrons and the material reveal the surface topography. The images of titanium dioxide sample are taken by FESEM. EDS can measure the elemental composition of the specimen. The ratio of tungsten in the samples is measured by EDS.

Chapter 4

Results and Discussion

4.1 Introduction

In this chapter, samples synthesized under the parameters shown in Fig 2.1 are studied. For three different cases, the bubbler temperature is kept at 90°C. The substrate height is kept at 1 inch, and the temperature of the surface of the collecting substrate stays at around 80°C with an accuracy of $\pm 5^\circ\text{C}$, measured by a type K thermocouple inserted between the cooling substrate and the collection substrate. The temperature of the substrate can be kept steady by adjusting the flow rate of the cooling water. As for all cases, the same precursor loading rate and concentration is maintained, running for 600 seconds (with no tungsten mesh, single layer of tungsten mesh, and double layers of tungsten mesh over the honeycomb). All powders are post-annealed at 973 K for 3 hours in Ar atmosphere. XRD, SEM, TEM, and UV-vis results of the as-synthesized and after heat-treatment samples are discussed and compared in this chapter.

4.2 XRD Results and Discussion

4.2.1 XRD results

The XRD patterns of as-synthesized and heat-treated un-doped and W-doped-TiO₂ nanopowders are shown in Fig 4.1. 1W stands for the powders collected using a single layer of tungsten mesh, and 2W stands for the double layers. HT stands for heat treatment process which is annealing in

Ar atmosphere for 3 hours at 700°C. Fig 4.2 shows the enlarged pattern of the anatase (101) and rutile (110) peaks of un-doped and doped TiO₂. Fig. 4.3a, b, c, d, e, and f show the parameters a and c , along with the cell volume of both anatase and rutile phases of all samples. The cell volume and parameters a and c are calculated by Rietveld refinement.

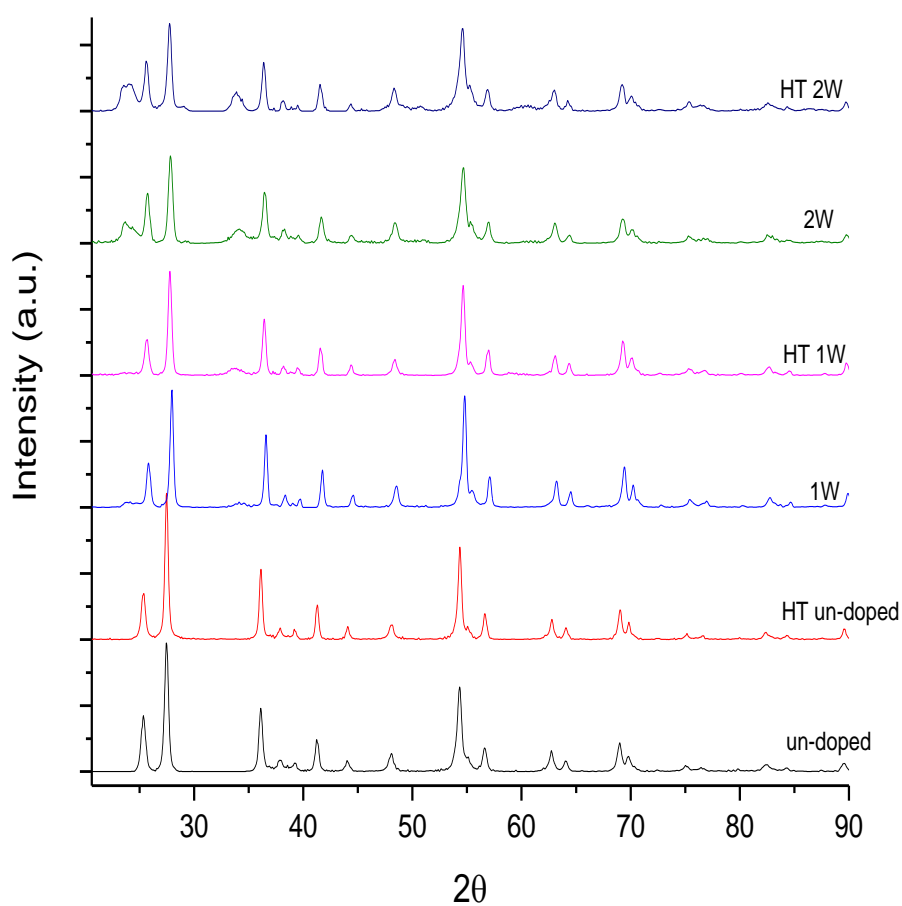


FIG 4.1 XRD pattern of as-synthesized and calcined doped/un-doped TiO₂

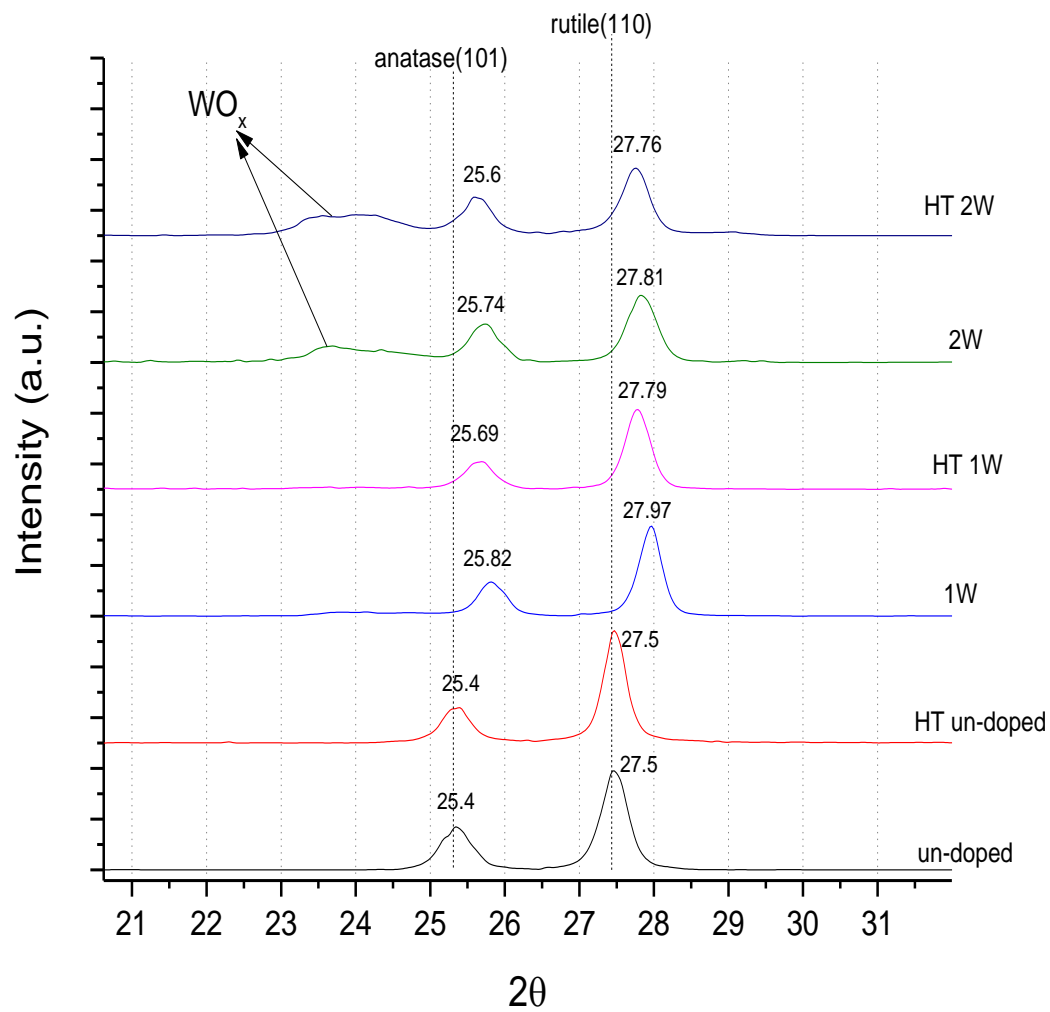


Fig 4.2 enlarged anatase (101) and rutile (110) peak

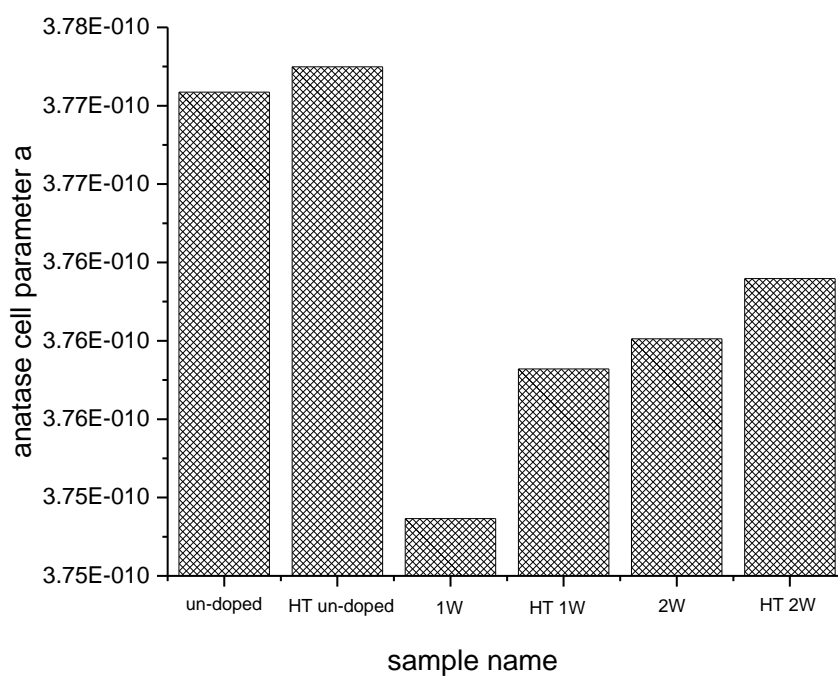


Fig 4.3a anatase parameter a

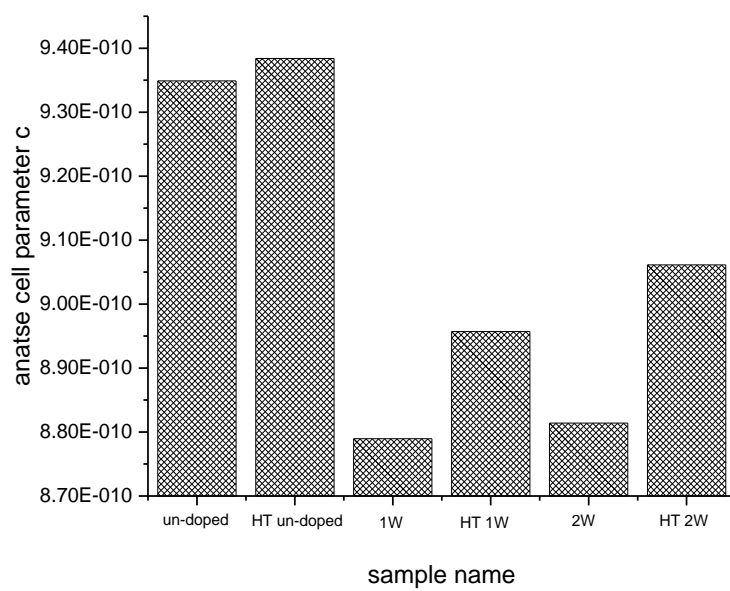


Fig 4.3b anatase parameter c

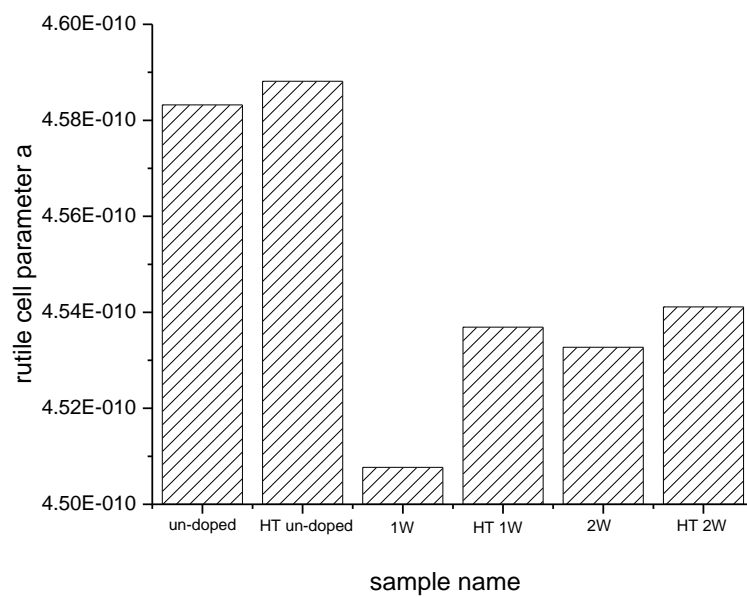


Fig 4.3c rutile parameter a

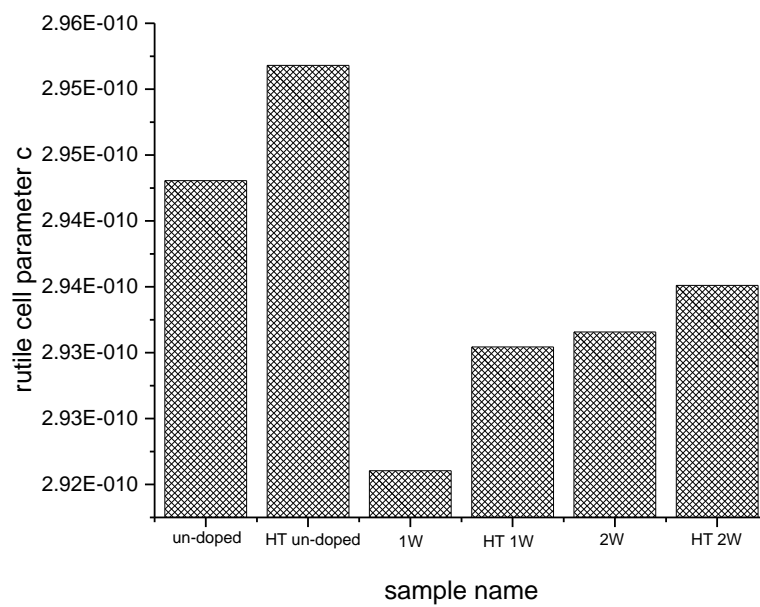


Fig 4.3d rutile parameter c

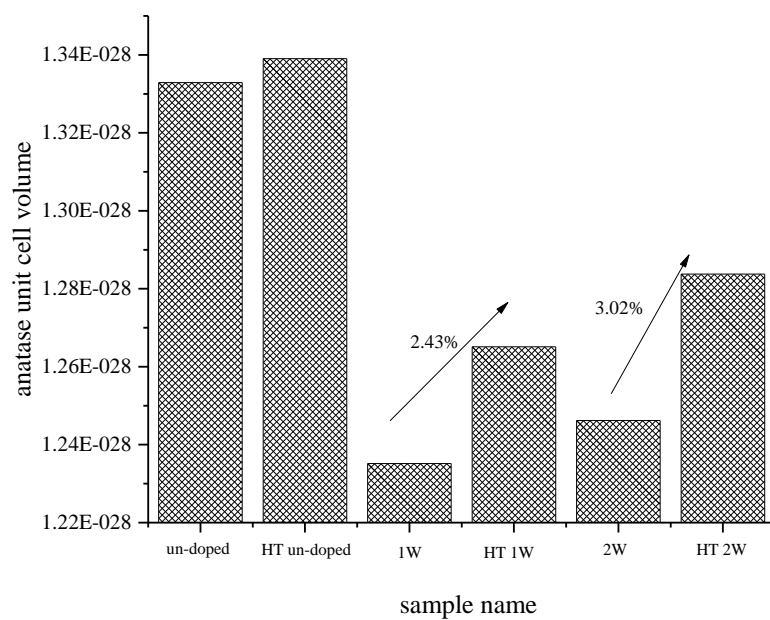


Fig 4.3e Anatase unit cell volume

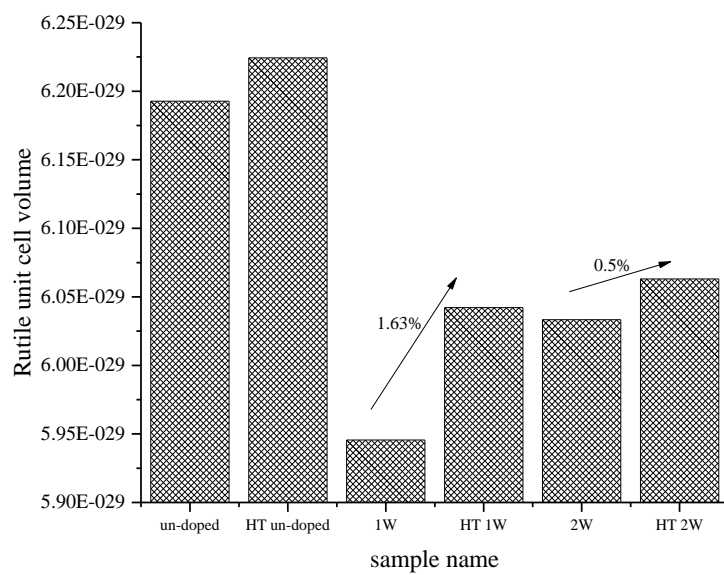


Fig 4.3f Rutile unit cell volume

4.2.2 XRD results discussion

It is notable that both as-synthesized and calcined un-doped TiO_2 match well with the X-ray diffraction angles (2θ) of 25.4 and 27.5, representing the (101) and (110) crystal planes of anatase and rutile, respectively. Meanwhile all W- TiO_2 nanoparticles have a shift to the right, for both as-synthesized and calcined, as annotated in **Fig 4.2**. We can easily see the WO_x peaks in the samples synthesized using double layers of tungsten mesh, while barely any WO_x is detected under XRD when using a single layer of tungsten mesh. However, both anatase and rutile peaks of 1W are shifted more degrees than for 2W. Also, parameters a and c , along with cell volume, decrease more, when comparing to the un-doped TiO_2 . Meanwhile, both anatase and rutile peaks of W- TiO_2 nanoparticles shift towards the un-doped TiO_2 after heat treatment. The reasons for this are discussed in this section.

4.2.2.1 Different shift angles between 1W and 2W

To better illustrate the reason why the shift angle is larger when using single layer of tungsten mesh as dopant source instead of double layers of tungsten, we start from the mechanisms of particle growth in flame synthesis.

Flame synthesis is gas phase synthesis where aerosol particles collide with each other to form larger particles. **Fig 4.4** shows a schematic of the mechanisms of particle formation and growth processes of gas-phase flame synthesis in sequence. In gas phase synthesis, when a thermodynamically unstable vapor phase mixture reaches supersaturation, vapor phase molecules start to form monomers and clusters. Clustering leads to homogeneous nucleation of particles, without the aid of any foreign surfaces. After nucleation, remaining supersaturation can be relieved

by condensation or surface reaction of the vapor phase molecules on the existing particles, and surface growth should outcompete nucleation. For vapor that has not reached supersaturation, particle formation and growth can be promoted by the presence of external nuclei, which is called heterogeneous nucleation. After the process of nucleation, the collision between two or more particles to make one larger particle that does not completely coalesce is known as agglomeration, and the resulting particle clusters are named agglomerates.

Coalescence is the final part when two or more particles fuse together to form a single spherical particle, where an aggregate particle will reduce its surface area over time while retaining all its mass. The competition between collision time and sintering time will determine whether the particles are aggregated or coalesced. For example if collision time is much smaller than sintering time, then aggregates will form; if sintering time is much smaller than collision time, then coalesced particles will form. In this experiment, when the TTIP is exposed to high flame temperatures, it pyrolyzes converts to TiO_2 monomers and clusters that grow. As the hot stream travels towards the cooling substrate, homogeneous nucleation occurs due to supersaturation resulting from the temperature drop, and the particles grow by coagulation, coalescence, and surface reactions. As the particles approach the cold substrate, agglomeration takes over with decreasing coalescence due to the lowering temperature, resulting in agglomerates or aggregates of particles (depending on the temperature history).

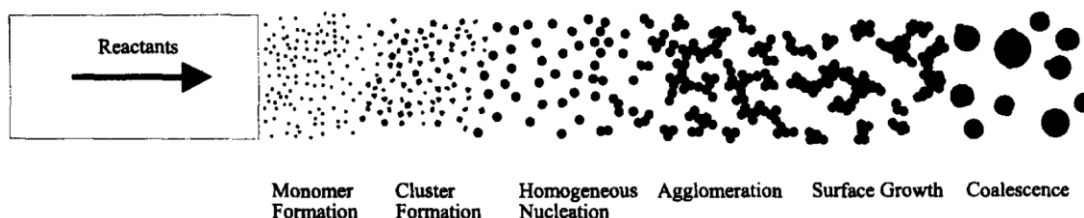


Fig 4.5 Particle formation and growth mechanisms⁷²

For the tungsten mesh as doping precursor, it will oxidize in the post-flame gases, and its oxides will be volatile enough to be transported into the gas phase. Depending on the relative supersaturation levels between these gas-phase species and the TiO_2 species, the tungsten oxides can dope in, coat on, or co-nucleate with the TiO_2 nanoparticles. As such, there are various parameters that can be adjusted to obtain the desired morphology/composition of nanoparticles. For example, if the gas-phase concentration of WO_x is much larger than that of TiO_2 , it may be possible to obtain Ti-doped tungsten oxide nanoparticles.

The homogeneous and heterogeneous nucleation mechanisms may explain the larger shift angle of the 1W powders. **Fig 4.4** shows that the 1W nanoparticles have a larger decrease in the unit cell volume than do the 2W nanoparticles, when compared to the un-doped TiO_2 nanoparticles, which corresponds with the fact that the peak shift of 1W in the XRD pattern is larger. Considering that the ionic radius W^{6+} has a smaller radius than Ti^{4+} , it is surmised that this is due to the larger amount of tungsten doped into the TiO_2 lattice.

When double layers of tungsten mesh are used as dopant source, the concentration is high enough such that the tungsten-oxide vapor is supersaturated before reaching the center TTIP flame area, so that WO_3 homogeneous nucleation initiates. Upon reaching the TTIP region, some of the W-based ions tended to form new agglomerates with TiO_2 , and the rest continue their growth as WO_3 . Thus W-based species are either coagulated with TiO_2 agglomerates or WO_3 aggregates, and W is not precipitated out.

For a single layer of W-mesh precursor, the tungsten-oxide vapor does not reach supersaturation prior to mixing with Ti-based species. As such, no WO_x nucleates are formed. Instead, W-based species can heterogeneously deposit on (concurrently and alternately with TiO_2

monomers) and dope into the TiO_2 nanoparticles. As we find neither WO_3 nor pure W peak in sample 1W's XRD pattern, all tungsten-oxide vapor seemingly goes into the TiO_2 lattice to form the W- TiO_2 particles. The EDS results in the later section will better prove our theory. **Fig 4.5** a and b show the general schematic of the nucleation process in the 1W and 2W situations.

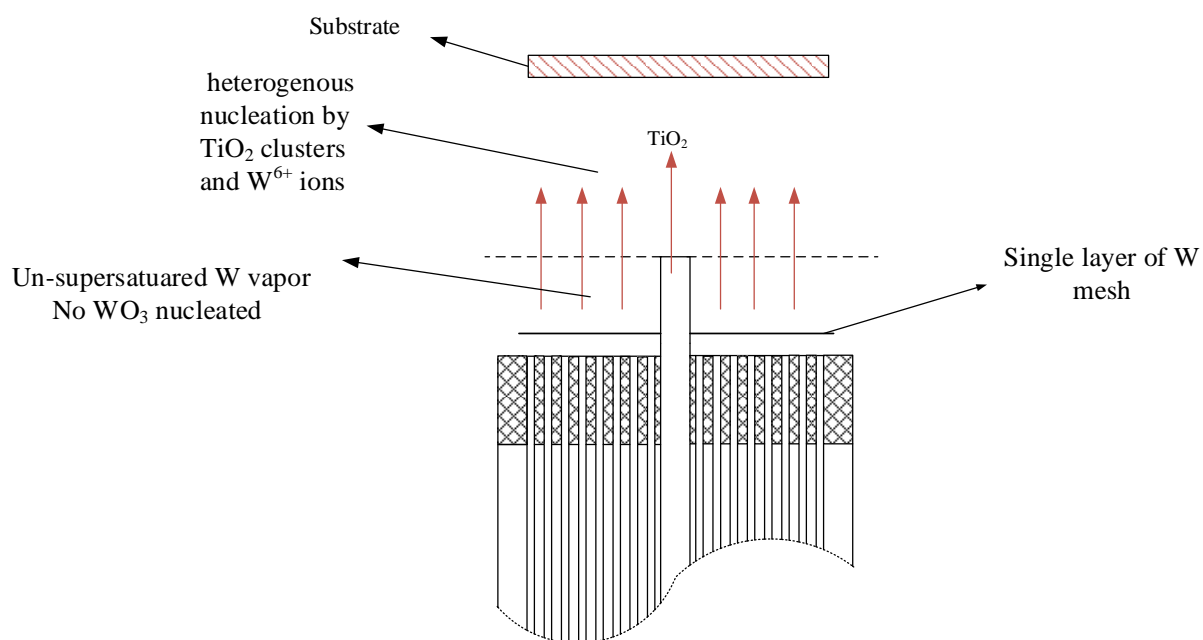


Fig 4.5a Heterogeneous nucleation using single layer W mesh

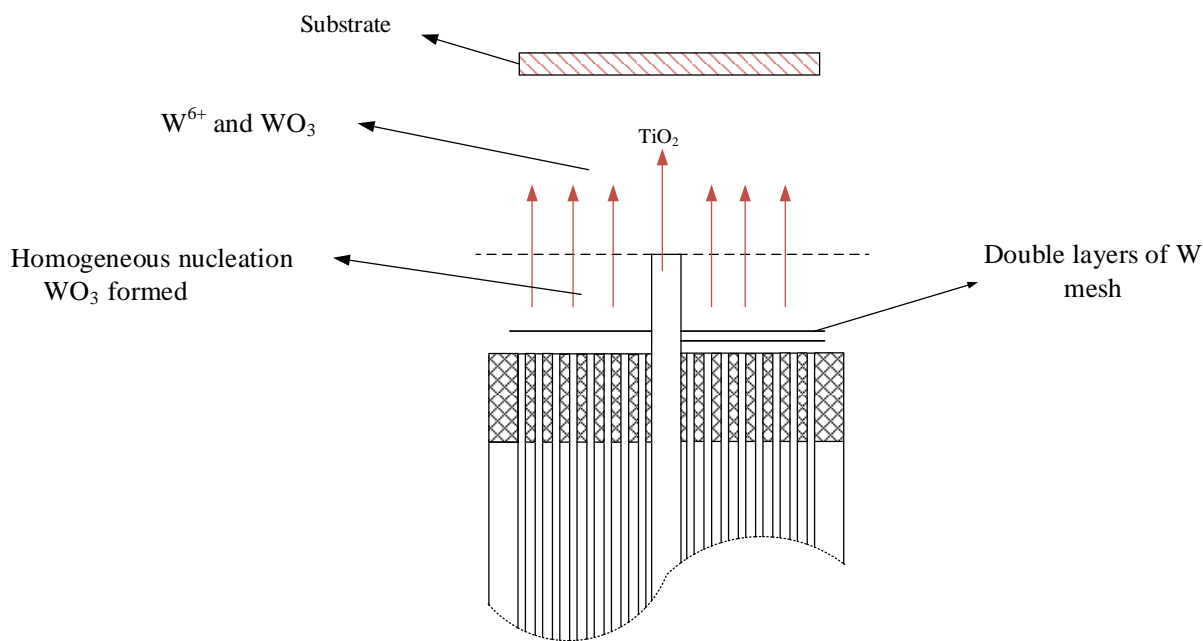


Fig 4.5b Homogenous nucleation using double layers W mesh

With the tungsten-oxide vapor pressure higher when using double layers of mesh, the self-nucleation of WO_x may leave fewer W-based species coagulated with the TiO_2 agglomerates, as compared to that for a single layer of mesh. As more tungsten is doped into TiO_2 , the Ti-O-W bond making the unit cell volume reduces, and thus the 1W peaks shifted more angles than 2W in XRD patterns.

4.2.2.2 WO_x peak and unit cell volume change after heat treatment

It is worth noting the WO_x peak differences between 2W and HT 2W. WO_x denoting is used for the peaks because the peak of 2W is a better match with WO_3 , while the peak of HT 2W is closer to $\text{W}_{18}\text{O}_{49}$. Leghari⁷³ et al. and other works^{74,75} reported that tungsten ions doped in TiO_2 can replace titanium ions to form new W-O-Ti bonds. Considering the decrease in the unit cell volume and parameters a and c of both anatase and rutile phases (**Fig 4.3**), it is likely that the tungsten ions

replaced the titanium ions here, thus making a new $\text{WO}_x\text{-TiO}_2$ solid solution based on the fact that W^{6+} (0.6 Å) has a smaller ionic radius than Ti^{4+} (0.61 Å). However, after annealing in Ar for 3 hours at 700°C, the W-TiO₂ unit cell volume and parameters a and c of both phases increased, becoming closer to that of the un-doped TiO₂ (**Fig 4.3**), matching the results from **Fig 4.2** that the HT peaks of both phases shifted back towards the un-doped nanopowders.

Despite the low diffusivity of W, the results seem to indicate migration of the tungsten within the TiO₂ structure due to the heat treatment, making the unit cell volume closer to the un-doped TiO₂. Tungsten moved to the surface of TiO₂ can exist in lower oxidation states, W^{4+} and W^{5+} , possibly explaining the trend of the WO_x peak change from WO_3 to $\text{W}_{18}\text{O}_{49}$, given that annealing in Ar where the amount of contained O^{2-} should stay the same. **Fig 4.3** shows that the anatase unit cell volume and parameters a and c of both 1W and 2W increase more by percentage (shown in **Fig 4.3d, f**) after heat treatment than those of rutile, which is the more stable phase in this high temperature environment.

4.3 SEM and EDS Results and Discussion

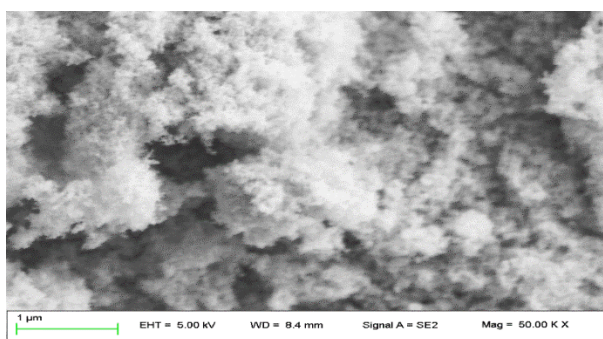


Fig 4.6a SEM image of un-doped TiO₂

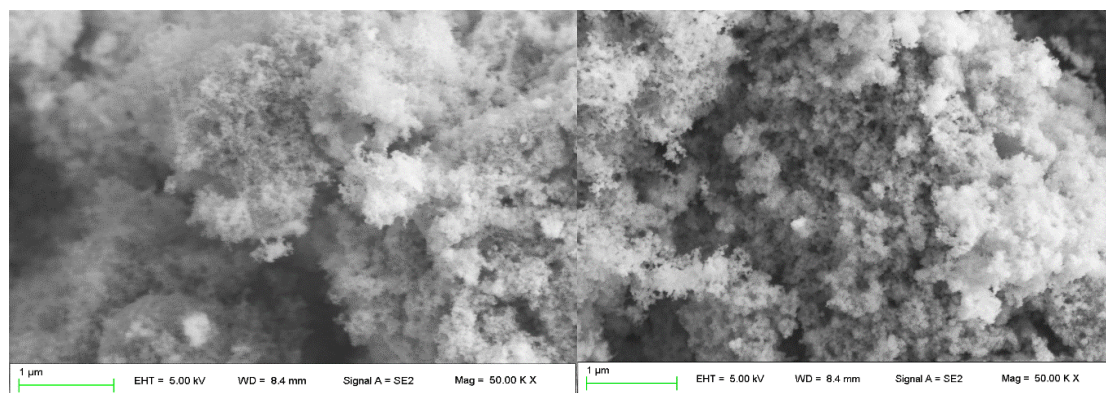


Fig 4.6b SEM images of TiO₂-1W (left) and HT-TiO₂-1W (right)

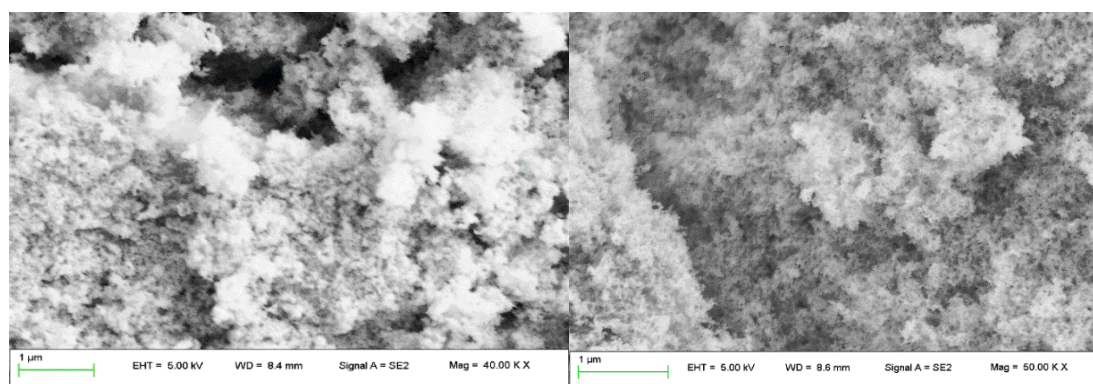
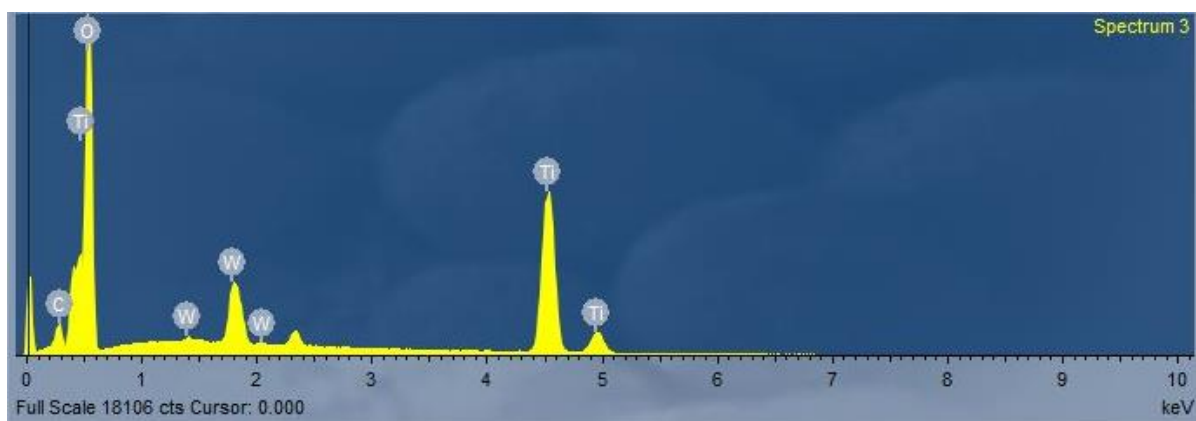
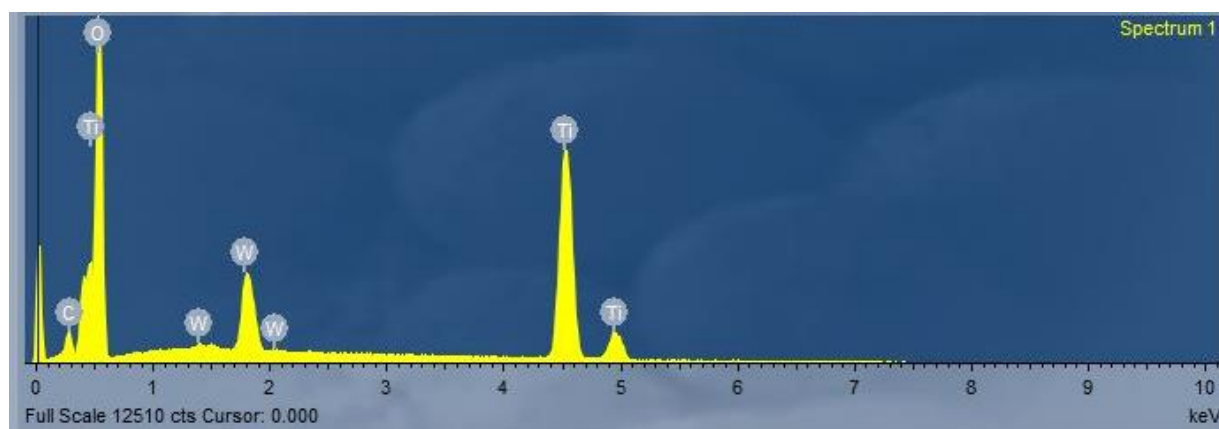
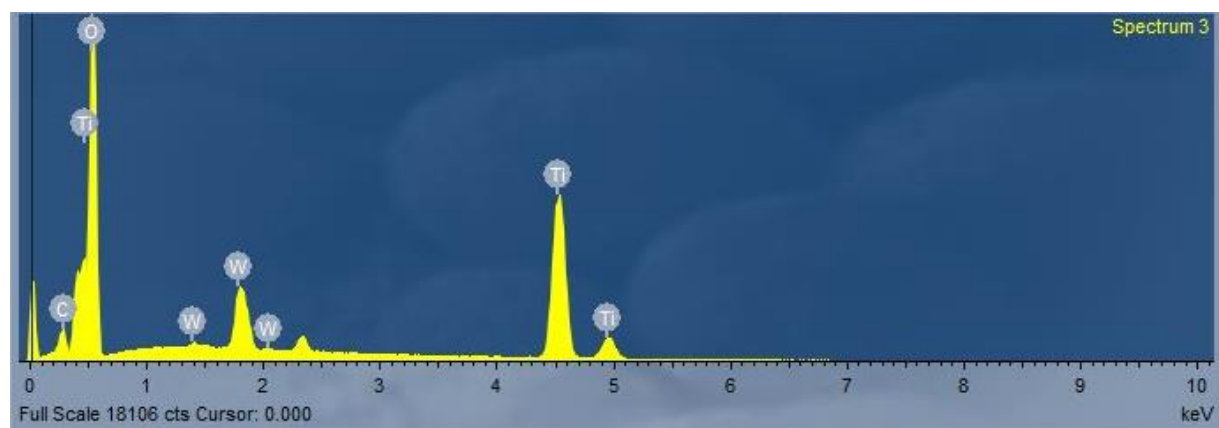
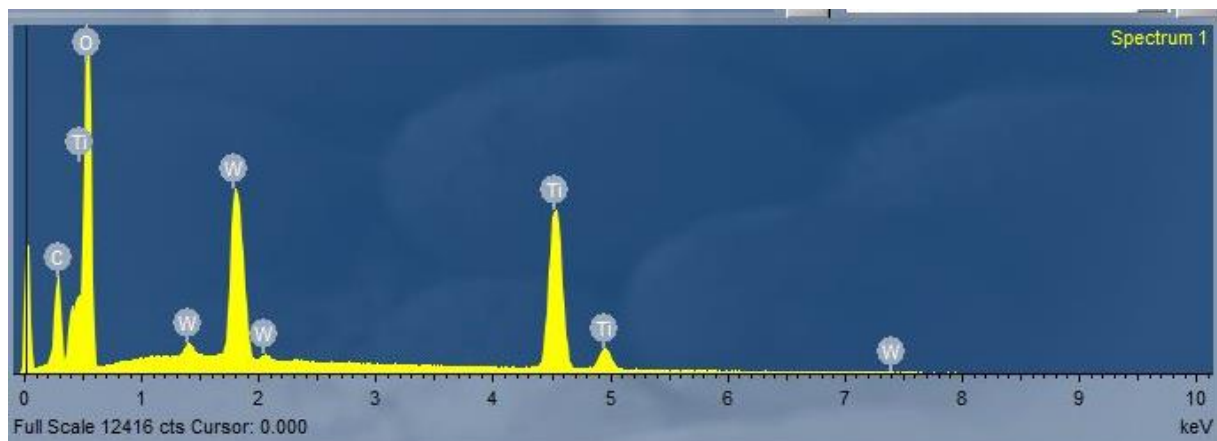


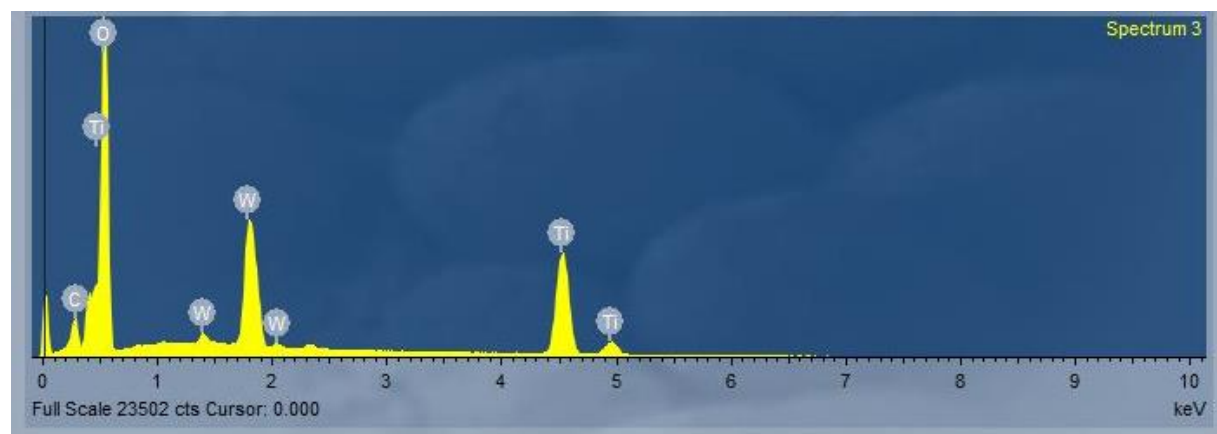
Fig 4.6c SEM images of TiO₂-2W (left) and HT-TiO₂-2W (right)

From the SEM images in **Fig 4.6**, the HT samples looked denser compared to the un-doped samples and those before HT. Un-doped TiO₂ looked fluffier. Although both W-doping and annealing appears to change the structure of TiO₂, they do not affect the morphology too much.

**a****b****c**



d



e

Fig 4.7 EDS spectrum of (a) un-doped TiO_2 , (b) TiO_2 -1W, (c) HT- TiO_2 -1W, (d) TiO_2 -2W, (e) HT- TiO_2 -2W

Noticing the C signal coming from the background, the weight and atomic percentages in W- TiO_2 powders are listed in **table 4.1**.

Sample	W weight %	W atomic %
TiO ₂ -1W	9.77	1.5
HT-TiO ₂ -1W	9.55	1.4
TiO ₂ -2W	21.5	3.39
HT-TiO ₂ -2W	22.2	3.38

Table 4.1 Weight and atomic percentage of tungsten

Clearly when using double layers of W mesh, there is more tungsten in the sample, mainly from WO₃ presence. The slight difference between the percentage before and after annealing might be caused by the un-balanced distribution of the powders. The difference is acceptable overall. As given in the previous section, neither WO₃ nor W are seen in the XRD pattern of sample TiO₂-1W, either before or after heat treatment. However, the EDS results seem to indicate that about 1.5% (atomic) tungsten exists in the powders. Therefore, apart from the W-based compounds existing in non-crystalline states, it is most likely that W is successfully doped into the lattice of TiO₂ nanoparticles.

4.4 XPS Results and Discussion

The XPS spectra of W 4*f* obtained from 1W and HT 1W nanopowders are depicted in **Fig 4.8**. The 1W-TiO₂ shows the W 4*f* binding energy at 38.48 and 36.38 eV, typical for the WO₃ chemical state. After heat treatment, the fitting analysis reveals that the tungsten is in the mixed valence

state, with binding energies at 38.58, 36.68, 35.38, and 33.08 eV. According to the NIST XPS database, the tungsten is reduced to lower oxidation states by the heat treatment. The XPS results match well with the results from XRD, where after heat treatment, some of the tungsten ions are replaced by titanium ions to form Ti-O bonds instead of W-O bonds, thus making the unit cell volume closer to the un-doped TiO_2 with tungsten ions reduced to lower oxidation states.

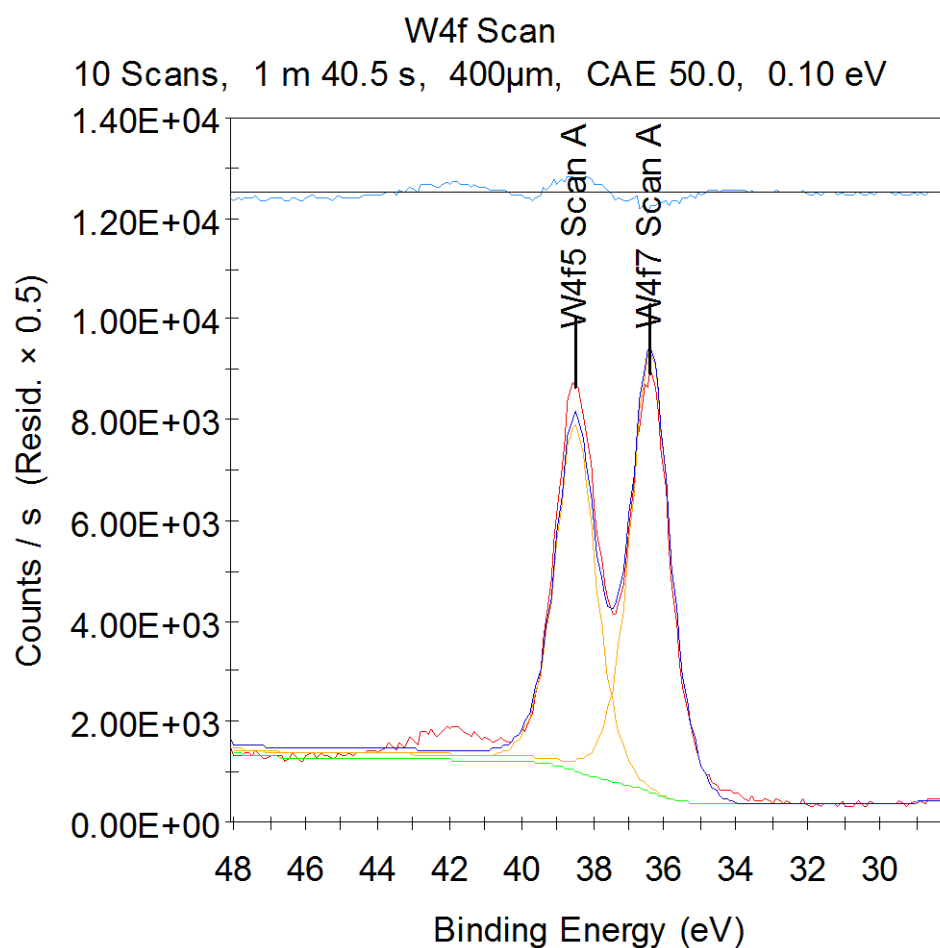


Fig 4.8a XPS spectra of W 4f core level of 1W-TiO₂

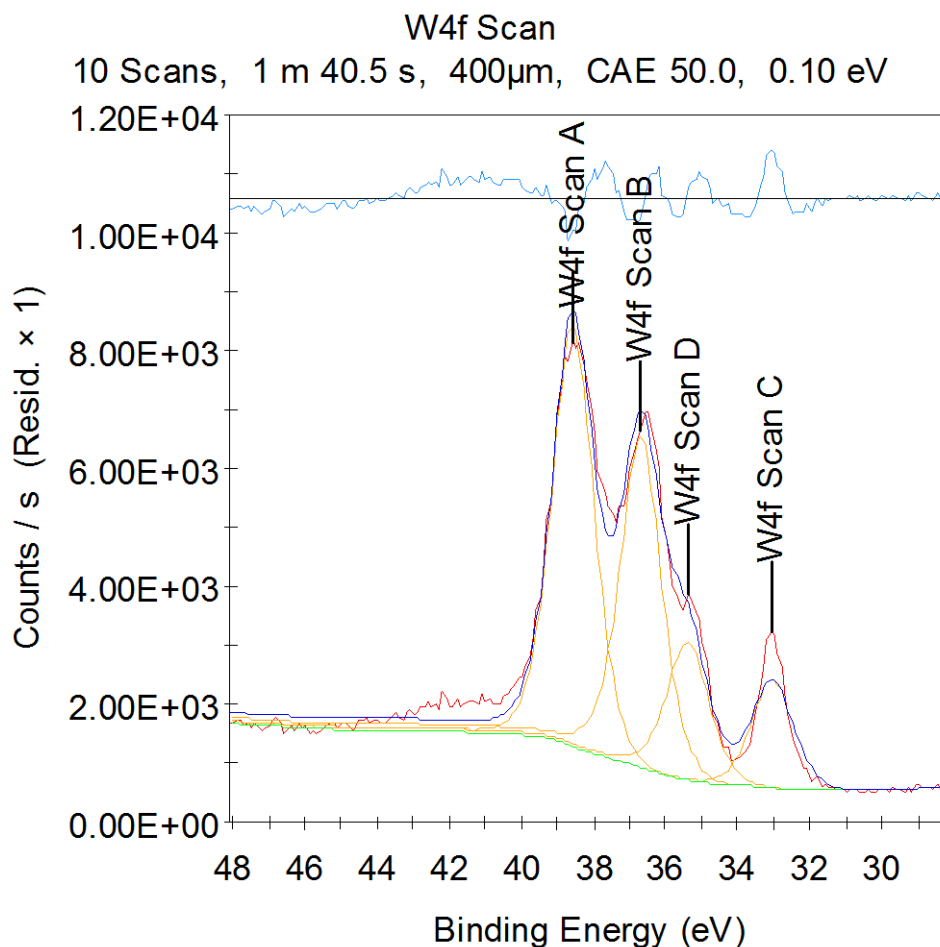


Fig 4.8b XPs spectra of W 4f core level of HT-1W-TiO₂

4.5 TEM Results and Discussion

Fig 4.9 shows the TEM and SAED patterns of 1W-TiO₂ nanoparticles. The average primary particles size is found by measuring 20 to 30 nanoparticles in the TEM image using software Digital Micrograph. The images reveal the average primary particle to be around 20 nm. Using the same software, the *d*-spacings are also measured, which are listed in **Table 4.2**. The *d*-spacing data from the XRD database are listed in **Table 4.3**. We notice that the 1W-TiO₂ nanoparticles have a slightly

decreased d -spacing, which corresponds with the unit cell volume decrease as discussed in an earlier section.

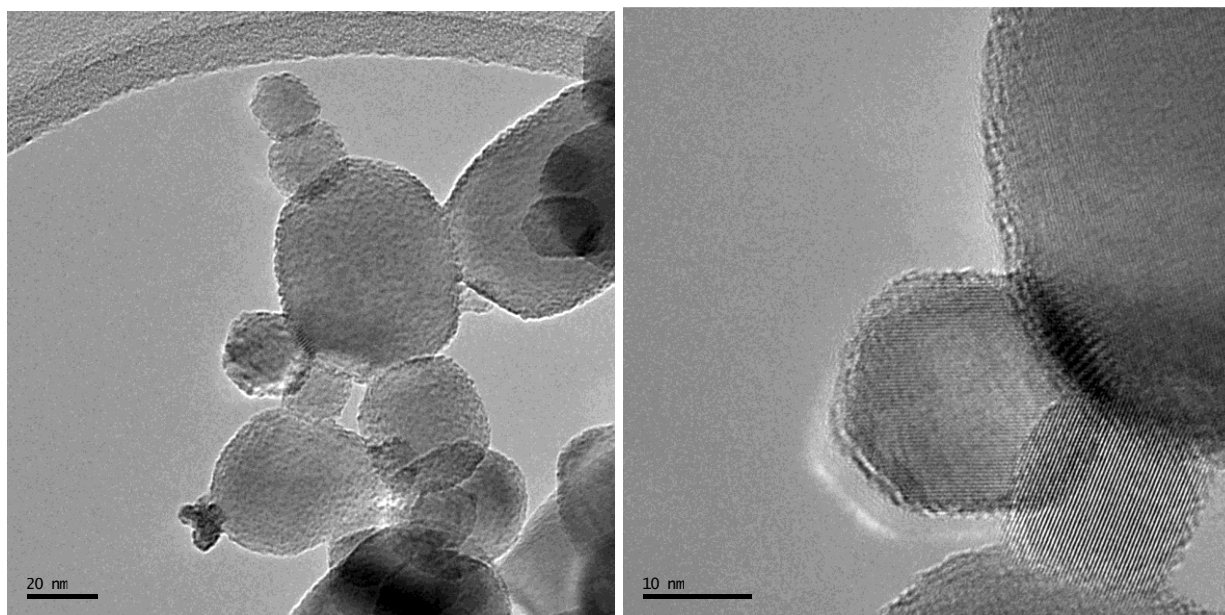


Fig4.9a TEM images of 1W-TiO₂ nanoparticles

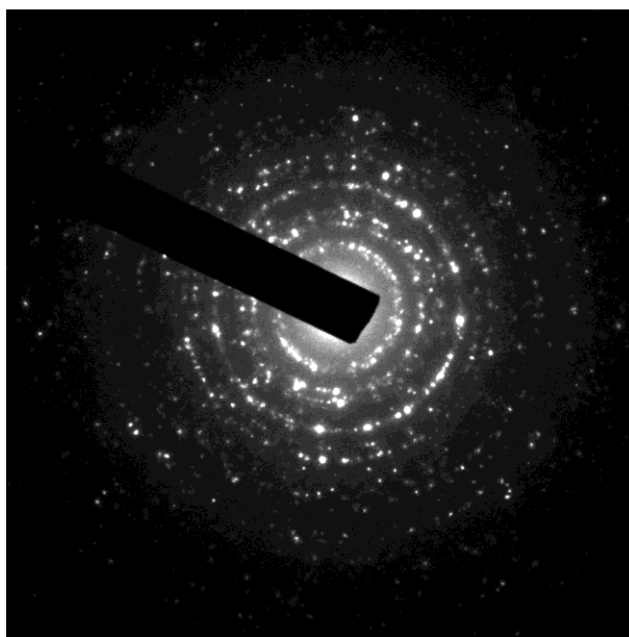


Fig 4.9b SAED patterns of 1W-TiO₂ nanoparticles

Phase	d-spacing(Å)
Anatase	3.491(101), 2.348(004), 1.871(200)
Rutile	3.223(110), 2.457(111), 1.664(211)

Table 4.2 Measured *d*-spacing of 1W-TiO₂

Phase	<i>d</i> -spacing(Å)
Anatase	3.516(101), 2.379(004), 1.892(200)
Rutile	3.249(110), 2.488(111), 1.688(211)

Table 4.3 *d*-spacing of un-doped TiO₂

4.6 UV-Vis Results and Discussion

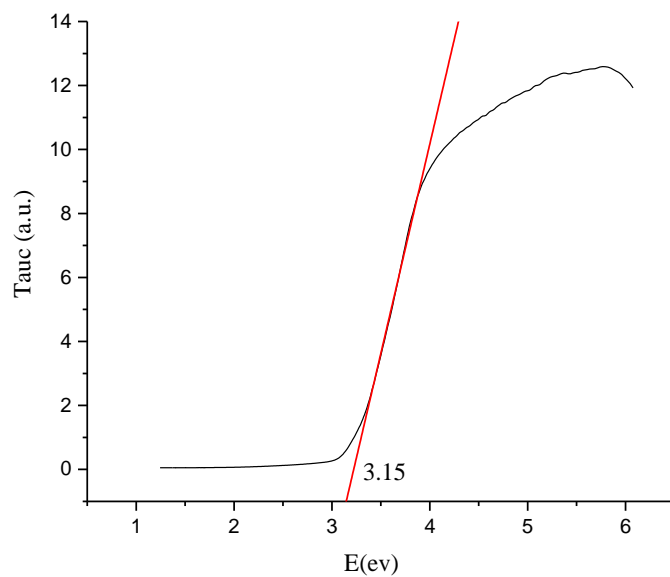


Fig 4.10a Tauc plot of un-doped TiO₂

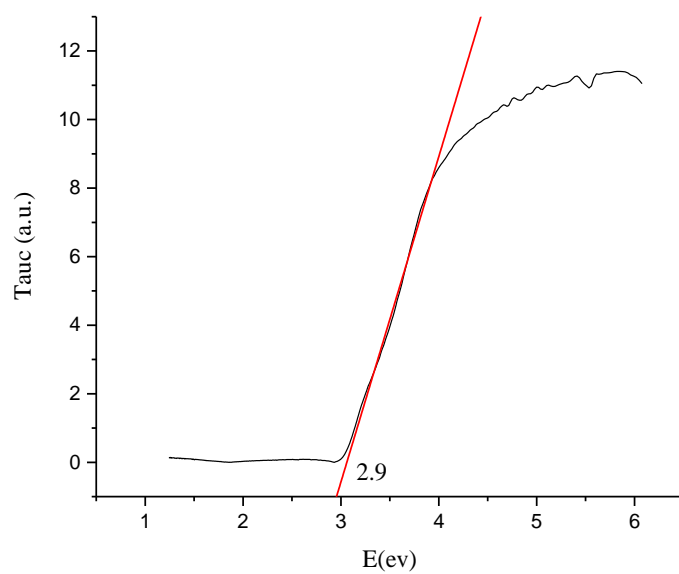


Fig 4.10b Tauc plot of 1W-TiO₂

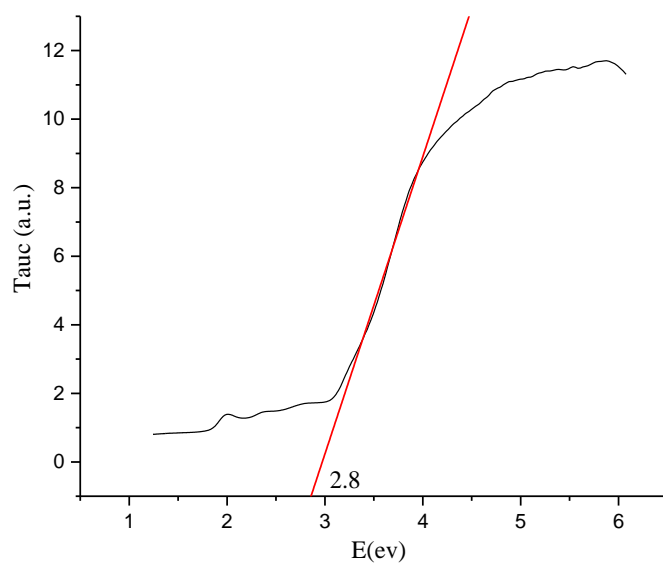


Fig 4.10c Tauc plot of HT-1W-TiO₂

The Tauc plots of un-doped TiO₂, 1W-TiO₂, and HT-1W-TiO₂ are shown in **Fig 4.10**. The intersection points of the tangent lines and the Tauc plot depict the band gap of the samples. The

1W-TiO₂ nanopowders have a lower band gap of 2.9 eV than do the un-doped TiO₂ (3.15 eV) nanopowders. After heat treatment, the band gap is even lower (2.8 eV). The lower band gap corresponds to better performance for visible-light photocatalytic reactions. The enhanced visible-light photoactivity of W-doped TiO₂ can be explained by a new energy level produced in the band gap of TiO₂ by the dispersion of metal ions in the TiO₂ matrix. Electron can be excited from the defect state to the TiO₂ conduction band by photon with lower energy since W-doping brings in more electrons into the TiO₂ lattice. As discussed in previous sections, according to the XPS results, tungsten ions are reduced to lower oxidation states by the heat treatment which exposes more free electrons in the nanopowders thus decreasing the band gap even more.

Chapter 5

Conclusions and Future Scope

5.1 Conclusions

Un-doped TiO_2 and W-doped TiO_2 are successfully synthesized by a multiple diffusion flames burner with a center tube carrying fuel and TTIP as the precursor. XRD patterns show a shifted angle for W-doped TiO_2 and WO_3 peak when the tungsten loading rate is high enough. However, high concentrations of tungsten-oxide can trigger homogenous nucleation of WO_3 before the stream reaches the TTIP precursor loaded center jet region, leaving less tungsten-based species to coated or doped composites with TiO_2 , as compared to that for lower tungsten-based loading rate conditions. Furthermore, EDS results show that although lower tungsten-based loading rate produce powders with almost 10% (weight) tungsten, neither WO_3 nor W are detected by XRD, demonstrating that tungsten is likely doped into the lattice of TiO_2 . Heat treatment at 973 K in the Ar atmosphere seems to move some the tungsten out of the TiO_2 chemical structure, making a new WO_x - TiO_2 solid solution with tungsten ions (at the surface) reduced to lower oxidation states. Moreover the annealing process also increases the unit cell volume of W-doped TiO_2 , making the value closer to that of the un-doped TiO_2 .

5.2 Future Scope

Most research by other workers using flame synthesis to produce TiO_2 have synthesized pure or almost pure anatase phase TiO_2 , while our experiments always produce both anatase and rutile

phases. With the rutile phase transformed from the anatase phase at high temperature and long residence time, in future studies, The temperature time history (including residence time) can be controlled by adjusting the distance to the substrate (for example, shortening it).

Some research has mentioned that doping of W can retard the phase transition from anatase to rutile during heat treatment. In this work annealing was performed for three hours. In future studies, the annealing time can be extended, as well as conducted under normal atmosphere, to explore the property changes.

Not only limited to tungsten, other metals, such as molybdenum and silver, can also be investigated for their doping into TiO_2 using the same method and set-up. Moreover, multiple metals can be doped into TiO_2 concurrently.

Chapter 6

References

1. Fujishima, A. Electrochemical photolysis of water at a semiconductor electrode. *nature* **238**, 37–38 (1972).
2. Carp, O., Huisman, C. L. & Reller, A. Photoinduced reactivity of titanium dioxide. *Prog. Solid State Chem.* **32**, 33–177 (2004).
3. Sang, L., Zhao, Y. & Burda, C. TiO₂ Nanoparticles as Functional Building Blocks. *Chem. Rev.* **114**, 9283–9318 (2014).
4. Gupta, S. M. & Tripathi, M. A review of TiO₂ nanoparticles. *Chin. Sci. Bull.* **56**, 1639–1657 (2011).
5. Cromer, D. T. & Herrington, K. The Structures of Anatase and Rutile. *J. Am. Chem. Soc.* **77**, 4708–4709 (1955).
6. Baur, W. H. Atomabstände und Bindungswinkel im Brookit, TiO₂. *Acta Crystallogr.* **14**, 214–216 (1961).
7. Mo, S.-D. & Ching, W. Y. Electronic and optical properties of three phases of titanium dioxide: Rutile, anatase, and brookite. *Phys. Rev. B* **51**, 13023–13032 (1995).
8. Diebold, U. The surface science of titanium dioxide. *Surf. Sci. Rep.* **48**, 53–229 (2003).
9. Chen, X. & Mao, S. S. Titanium dioxide nanomaterials: synthesis, properties, modifications, and applications. *Chem. Rev.* **107**, 2891–2959 (2007).
10. Thompson, T. L. & Yates, J. T. Surface science studies of the photoactivation of TiO₂ new photochemical processes. *Chem. Rev.* **106**, 4428–4453 (2006).
11. Zhang, Q., Gao, L. & Guo, J. Effects of calcination on the photocatalytic properties of nanosized TiO₂ powders prepared by TiCl₄ hydrolysis. *Appl. Catal. B Environ.* **26**, 207–215 (2000).
12. Sclafani, A., Palmisano, L. & Schiavello, M. Influence of the preparation methods of titanium dioxide on the photocatalytic degradation of phenol in aqueous dispersion. *J. Phys. Chem.* **94**, 829–832 (1990).
13. Muscat, J., Swamy, V. & Harrison, N. M. First-principles calculations of the phase stability of TiO₂. *Phys. Rev. B* **65**, 224112 (2002).
14. Tanaka, K., Capule, M. F. & Hisanaga, T. Effect of crystallinity of TiO₂ on its photocatalytic action. *Chem. Phys. Lett.* **187**, 73–76 (1991).
15. Szacilowski, K., Macyk, W., Drzewiecka-Matuszek, A., Brindell, M. & Stochel, G. Bioinorganic photochemistry: frontiers and mechanisms. *Chem. Rev.* **105**, 2647–2694 (2005).
16. Li, G., Chen, L., Graham, M. E. & Gray, K. A. A comparison of mixed phase titania photocatalysts prepared by physical and chemical methods: the importance of the solid–solid interface. *J. Mol. Catal. Chem.* **275**, 30–35 (2007).
17. Pierre, A. C. & Pajonk, G. M. Chemistry of aerogels and their applications. *Chem. Rev.* **102**, 4243–4266 (2002).

18. Lu, Z., Lindner, E. & Mayer, H. A. Applications of sol-gel-processed interphase catalysts. *Chem. Rev.* **102**, 3543–3578 (2002).
19. Bessekhoud, Y., Robert, D. & Weber, J. V. Synthesis of photocatalytic TiO₂ nanoparticles: optimization of the preparation conditions. *J. Photochem. Photobiol. Chem.* **157**, 47–53 (2003).
20. Chemseddine, A. & Moritz, T. Nanostructuring titania: control over nanocrystal structure, size, shape, and organization. *Eur. J. Inorg. Chem.* **1999**, 235–245 (1999).
21. Burnside, S. D. *et al.* Self-organization of TiO₂ nanoparticles in thin films. *Chem. Mater.* **10**, 2419–2425 (1998).
22. Sugimoto, T., Zhou, X. & Muramatsu, A. Synthesis of uniform anatase TiO₂ nanoparticles by gel–sol method: 1. Solution chemistry of Ti (OH)_n (4–n)⁺ complexes. *J. Colloid Interface Sci.* **252**, 339–346 (2002).
23. Sugimoto, T., Okada, K. & Itoh, H. Synthetic of uniform spindle-type titania particles by the gel–sol method. *J. Colloid Interface Sci.* **193**, 140–143 (1997).
24. Uekawa, N., Kajiwara, J., Kakegawa, K. & Sasaki, Y. Low temperature synthesis and characterization of porous anatase TiO₂ nanoparticles. *J. Colloid Interface Sci.* **250**, 285–290 (2002).
25. Li, Y., White, T. J. & Lim, S. H. Low-temperature synthesis and microstructural control of titania nano-particles. *J. Solid State Chem.* **177**, 1372–1381 (2004).
26. Banfield, J. & others. Thermodynamic analysis of phase stability of nanocrystalline titania. *J. Mater. Chem.* **8**, 2073–2076 (1998).
27. Zhang, H. & Banfield, J. F. Understanding polymorphic phase transformation behavior during growth of nanocrystalline aggregates: insights from TiO₂. *J. Phys. Chem. B* **104**, 3481–3487 (2000).
28. Zhang, H., Finnegan, M. & Banfield, J. F. Preparing single-phase nanocrystalline anatase from amorphous titania with particle sizes tailored by temperature. *Nano Lett.* **1**, 81–85 (2001).
29. Zhang, H. & Banfield, J. F. Kinetics of crystallization and crystal growth of nanocrystalline anatase in nanometer-sized amorphous titania. *Chem. Mater.* **14**, 4145–4154 (2002).
30. Znaidi, L., Seraphimova, R., Bocquet, J. F., Colbeau-Justin, C. & Pommier, C. A semi-continuous process for the synthesis of nanosize TiO₂ powders and their use as photocatalysts. *Mater. Res. Bull.* **36**, 811–825 (2001).
31. Do Kim, K. & Kim, H. T. Synthesis of TiO₂ nanoparticles by hydrolysis of TEOT and decrease of particle size using a two-stage mixed method. *Powder Technol.* **119**, 164–172 (2001).
32. Graetzel, M. & Howe, R. F. Electron paramagnetic resonance studies of doped titanium dioxide colloids. *J. Phys. Chem.* **94**, 2566–2572 (1990).
33. Choi, W., Termin, A. & Hoffmann, M. R. The role of metal ion dopants in quantum-sized TiO₂: correlation between photoreactivity and charge carrier recombination dynamics. *J. Phys. Chem.* **98**, 13669–13679 (1994).
34. Maruska, H. P. & Ghosh, A. K. Transition-metal dopants for extending the response of titanate photoelectrolysis anodes. *Sol. Energy Mater.* **1**, 237–247 (1979).
35. Li, R., Chen, W. & Wang, W. Magnetoswitchable controlled photocatalytic system using ferromagnetic Fe⁰-doped titania nanorods photocatalysts with enhanced photoactivity. *Sep. Purif. Technol.* **66**, 171–176 (2009).

36. Ohno, T., Mitsui, T. & Matsumura, M. Photocatalytic Activity of S-doped TiO₂ Photocatalyst under Visible Light. *Chem. Lett.* **32**, 364–365 (2003).
37. Liu, Y., Chen, X., Li, J. & Burda, C. Photocatalytic degradation of azo dyes by nitrogen-doped TiO₂ nanocatalysts. *Chemosphere* **61**, 11–18 (2005).
38. Yu, J. C., Zhang, L., Zheng, Z. & Zhao, J. Synthesis and characterization of phosphated mesoporous titanium dioxide with high photocatalytic activity. *Chem. Mater.* **15**, 2280–2286 (2003).
39. Zaleska, A. Doped-TiO₂: A Review. *Recent Pat. Eng.* **2**, 157–164 (2008).
40. Zhao, Z. & Liu, Q. Mechanism of higher photocatalytic activity of anatase TiO₂ doped with nitrogen under visible-light irradiation from density functional theory calculation. *J. Phys. Appl. Phys.* **41**, 025105 (2008).
41. Lee, M. S., Hong, S.-S. & Mohseni, M. Synthesis of photocatalytic nanosized TiO₂-Ag particles with sol-gel method using reduction agent. *J. Mol. Catal. Chem.* **242**, 135–140 (2005).
42. Carneiro, J. O. *et al.* Study of the deposition parameters and Fe-dopant effect in the photocatalytic activity of TiO₂ films prepared by dc reactive magnetron sputtering. *Vacuum* **78**, 37–46 (2005).
43. Akurati, K. K. *et al.* Flame-made WO₃/TiO₂ nanoparticles: Relation between surface acidity, structure and photocatalytic activity. *Appl. Catal. B Environ.* **79**, 53–62 (2008).
44. Li, F. B. & Li, X. Z. The enhancement of photodegradation efficiency using Pt-TiO₂ catalyst. *Chemosphere* **48**, 1103–1111 (2002).
45. Li, X. Z. & Li, F. B. Study of Au/Au³⁺-TiO₂ photocatalysts toward visible photooxidation for water and wastewater treatment. *Environ. Sci. Technol.* **35**, 2381–2387 (2001).
46. Wu, Z., Dong, F., Zhao, W. & Guo, S. Visible light induced electron transfer process over nitrogen doped TiO₂ nanocrystals prepared by oxidation of titanium nitride. *J. Hazard. Mater.* **157**, 57–63 (2008).
47. Asahi, R., Morikawa, T., Ohwaki, T., Aoki, K. & Taga, Y. Visible-light photocatalysis in nitrogen-doped titanium oxides. *science* **293**, 269–271 (2001).
48. Takeshita, K. *et al.* Transient IR absorption study of charge carriers photogenerated in sulfur-doped TiO₂. *J. Photochem. Photobiol. Chem.* **177**, 269–275 (2006).
49. Lettmann, C., Hildenbrand, K., Kisch, H., Macyk, W. & Maier, W. F. Visible light photodegradation of 4-chlorophenol with a coke-containing titanium dioxide photocatalyst. *Appl. Catal. B Environ.* **32**, 215–227 (2001).
50. Zaleska, A., Sobczak, J. W., Grabowska, E. & Hupka, J. Preparation and photocatalytic activity of boron-modified TiO₂ under UV and visible light. *Appl. Catal. B Environ.* **78**, 92–100 (2008).
51. K\Horösi, L. & Dékány, I. Preparation and investigation of structural and photocatalytic properties of phosphate modified titanium dioxide. *Colloids Surf. Physicochem. Eng. Asp.* **280**, 146–154 (2006).
52. Prairie, M. R., Evans, L. R. & Martinez, S. L. Destruction of organics and removal of heavy metals in water via TiO₂ photocatalysis. in *Chemical oxidation: Technology for the nineties. Second international symposium* 428–441 (1992). at [https://books.google.com/books?hl=en&lr=&id=lxYkpazyLLIC&oi=fnd&pg=PA428&dq=Destruction+of+organics+and+removal+of+heavy+metals+in+water+via+TiO₂,+photocatalysis+in+chemi-](https://books.google.com/books?hl=en&lr=&id=lxYkpazyLLIC&oi=fnd&pg=PA428&dq=Destruction+of+organics+and+removal+of+heavy+metals+in+water+via+TiO2,+photocatalysis+in+chemi-)

+cal+oxidation:+Technology+for+the+nineties.+&ots=QctFl7oRPd&sig=BNSFZRZn0-wpYtmLg17PU_RB5iU>

53. Mahmoodi, N. M. & Arami, M. Degradation and toxicity reduction of textile wastewater using immobilized titania nanophotocatalysis. *J. Photochem. Photobiol. B* **94**, 20–24 (2009).
54. Asmussen, R. M., Tian, M. & Chen, A. A new approach to wastewater remediation based on bifunctional electrodes. *Environ. Sci. Technol.* **43**, 5100–5105 (2009).
55. Duonghong, D., Borgarello, E. & Graetzel, M. Dynamics of light-induced water cleavage in colloidal systems. *J. Am. Chem. Soc.* **103**, 4685–4690 (1981).
56. Abe, R., Sayama, K. & Sugihara, H. Effect of water/acetonitrile ratio on dye-sensitized photocatalytic H₂ evolution under visible light irradiation. *J. Sol. Energy Eng.* **127**, 413–416 (2005).
57. O'regan, B. & Grätzel, M. A low-cost, high-efficiency solar cell based on dye-sensitized colloidal TiO₂ films. *nature* **353**, 737–740 (1991).
58. Mor, G. K., Carvalho, M. A., Varghese, O. K., Pishko, M. V. & Grimes, C. A. A room-temperature TiO₂-nanotube hydrogen sensor able to self-clean photoactively from environmental contamination. *J. Mater. Res.* **19**, 628–634 (2004).
59. Sotter, E., Vilanova, X., Llobet, E., Stankova, M. & Correig, X. Niobium-doped titania nanopowders for gas sensor applications. *J. Optoelectron Adv Mater* **7**, (2005).
60. Ruiz, A. M., Cornet, A. & Morante, J. R. Performances of La–TiO₂ nanoparticles as gas sensing material. *Sens. Actuators B Chem.* **111**, 7–12 (2005).
61. Garzella, C. *et al.* Novel selective ethanol sensors: W/TiO₂ thin films by sol–gel spin-coating. *Sens. Actuators B Chem.* **93**, 495–502 (2003).
62. Zhao, H., Liu, X. & Stephen, D. T. Effects of pressure and precursor loading in the flame synthesis of titania nanoparticles. *J. Aerosol Sci.* **40**, 919–937 (2009).
63. Wang, J., Li, S., Yan, W., Stephen, D. T. & Yao, Q. Synthesis of TiO₂ nanoparticles by premixed stagnation swirl flames. *Proc. Combust. Inst.* **33**, 1925–1932 (2011).
64. Pratsinis, S. E., Zhu, W. & Vemury, S. The role of gas mixing in flame synthesis of titania powders. *Powder Technol.* **86**, 87–93 (1996).
65. Yeh, C. L., Yeh, S. H. & Ma, H. K. Flame synthesis of titania particles from titanium tetrakisopropoxide in premixed flames. *Powder Technol.* **145**, 1–9 (2004).
66. Hung, C.-H. & Katz, J. L. Formation of mixed oxide powders in flames: Part I. TiO₂-SiO₂. *J. Mater. Res.* **7**, 1861–1869 (1992).
67. George, A. P., Murley, R. D. & Place, E. R. Formation of TiO₂ aerosol from the combustion supported reaction of TiCl₄ and O₂. in *Faraday Symposia of the Chemical Society* **7**, 63–71 (Royal Society of Chemistry, 1973).
68. McCormick, J. R., Zhao, B., Rykov, S. A., Wang, H. & Chen, J. G. Thermal stability of flame-synthesized anatase TiO₂ nanoparticles. *J. Phys. Chem. B* **108**, 17398–17402 (2004).
69. Bhanwala, A. K., Kumar, A., Mishra, D. P. & Kumar, J. Flame aerosol synthesis and characterization of pure and carbon coated titania nano powder. *J. Aerosol Sci.* **40**, 720–730 (2009).
70. Fotou, G. P., Vemury, S. & Pratsinis, S. E. Synthesis and evaluation of titania powders for photodestruction of phenol. *Chem. Eng. Sci.* **49**, 4939–4948 (1994).
71. Akurati, K. K. *et al.* Synthesis of non-aggregated titania nanoparticles in atmospheric pressure diffusion flames. *Powder Technol.* **165**, 73–82 (2006).

72. Wooldridge, M. S. Gas-phase combustion synthesis of particles. *Prog. Energy Combust. Sci.* **24**, 63–87 (1998).
73. Leghari, S. A. K., Sajjad, S., Chen, F. & Zhang, J. WO₃/TiO₂ composite with morphology change via hydrothermal template-free route as an efficient visible light photocatalyst. *Chem. Eng. J.* **166**, 906–915 (2011).
74. Štengl, V., Velická, J., Maríková, M. & Grygar, T. M. New generation photocatalysts: how tungsten influences the nanostructure and photocatalytic activity of TiO₂ in the UV and visible regions. *ACS Appl. Mater. Interfaces* **3**, 4014–4023 (2011).
75. Aryanpour, M., Hoffmann, R. & DiSalvo, F. J. Tungsten-doped titanium dioxide in the rutile structure: theoretical considerations. *Chem. Mater.* **21**, 1627–1635 (2009).